JM PAPERS

Energy and dissipation spectra of waves propagating in the inner surf zone

Philippe Bonneton†

UMR 5805 EPOC, CNRS – University of Bordeaux, Allée Geoffroy Saint-Hilaire, F-33615 Pessac, France

The spectral behaviour of random sawtooth waves propagating in the inner surf zone is investigated in this study. We show that the elevation energy spectrum exhibits a universal shape with an ω^{-2} tendency in the inertial subrange and an exponential decay in the diffusive subrange (ω being the angular frequency). A theoretical spectrum is derived based on the similarities between sawtooth waves in the inner surf zone and Burgers wave solutions. Very good agreement is shown between this theoretical spectrum and laboratory experiments covering a large range of incident random wave conditions. Additionally, an equation describing the universal shape of the dissipation spectrum is derived. It highlights that the dissipation spectrum is nearly constant in the inertial subrange, consistent with prior laboratory observations. The findings presented in this study can be useful to improve broken wave dissipation parametrizations in stochastic spectral wave models.

Key words: shallow water flows, surface gravity waves

1. Introduction

Understanding the spectral behaviour of oceanic waves is crucial for the development of wave forecasting models. Analysing the shape of wave spectra provides a deeper comprehension of nonlinear and dissipation processes in the wavenumber or frequency domain. Moreover, it aids in identifying the key physical parameters that govern the dynamics of random wave fields. While the spectral characteristics of waves in deep and intermediate water are relatively well understood, this is not the case in the surf zone, where waves are controlled by strongly nonlinear and dissipative processes.

For well-developed seas in deep water, one can identify an equilibrium range in the energy spectrum that results from a constant flux of energy towards high frequencies. Hasselmann ([1962](#)) showed that this energy cascade is due to weakly nonlinear

† Email address for correspondence: philippe.bonneton@u-bordeaux.fr

four-wave interactions. Zakharov & Filonenko (1966) demonstrated theoretically, from the Hasselmann kinetic equation, that the equilibrium range is characterized by a universal power law of the shape ω^{-4} (where ω is the angular frequency). This law was confirmed by Toba (1973) from field observations. It was then shown that two frequency subranges coexist in the energy spectrum (e.g. Forristall 1981; Kitaigorodskii 1983; Hansen *et al.* 1990; Romero & Melville 2010; Lenain & Melville 2017): the equilibrium spectrum for $\omega_1 < \omega < \omega_2$, and a dissipative subrange for high frequencies ($\omega > \omega_2$), where the frequency bounds are given approximately by $\omega_1 \simeq 1.3$–$1.5\omega_p$ and $\omega_2 \simeq 3$–$3.6\omega_p$ (where ω_p is the peak frequency). Spectra follow an ω^{-5} power law in the dissipative subrange, the so-called Phillips spectrum (Phillips 1958), which results from a balance between weakly nonlinear four-wave interactions and dissipative processes.

As waves propagate shoreward in decreasing water depth, frequency dispersion decreases and triad interactions approach resonance. This results in an intense amplification of the harmonics of the spectral peak, over distances of only a few wavelengths (Freilich & Guza 1984; Elgar & Guza 1985*b*). The spectral shape thus displays strong variability in space. In this context, it is questionable whether these waves can be characterized by an equilibrium spectrum. Kitaigordskii, Krasitskii & Zaslavskii (1975) and Thornton (1977), using similarity arguments in line with Phillips (1958), suggested that the high-frequency portion of the spectrum follows an ω^{-3} power law in the shoaling zone . Although field observations show that the characteristic high-frequency spectral slope (between -3 and -4, approximately) is less steep than in deep water (ω^{-5} Phillips spectrum), there is no clear evidence of a universal power-law spectrum.

As waves move through the surf zone, the nonlinear interactions tend to redistribute the energy around local peaks in the spectrum. The high-frequency portion of the spectrum thus evolves gradually into a flat, featureless shape (Herbers & Burton 1997; Kaihatu *et al.* 2007). Smith & Vincent (2003) proposed a parametrization of the high-frequency range based on the analysis of laboratory and field data. Their parametrization, expressed in the wavenumber space, consists of two power laws: $k^{-4/3}$ for $2.5k_p < k < 1/h_0$, and $k^{-5/2}$ for $k > 1/h_0$, where k is the wavenumber, k_p is the wavenumber at the spectral peak, and h_0 is the mean water depth. Smith & Vincent (2003) referred to the shallow-water theory of Zakharov (1999) for the first law, and to the deep-water Toba's spectrum (derived theoretically by Zakharov & Filonenko 1966) for the second law. This is questionable because waves in the surf zone are strongly nonlinear and beyond the scope of the weakly nonlinear theories by Zakharov (1999) and Zakharov & Filonenko (1966). Moreover, Smith & Vincent (2003) used a transformation of the observed frequency spectrum $E(\omega)$ into a wavenumber spectrum $E(k)$ based on the linear dispersive relation. In the surf zone, this relation strongly overestimates k for high frequencies (Thornton & Guza 1982; Martins, Bonneton & Michallet 2021). The linear transformation thus leads to an artificial stretching of $E(k)$ towards high wavenumbers, making the $k^{-5/2}$ power law highly questionable. Therefore, until now, there is no clear evidence of universal spectral power laws, in the wavenumber space, for the surf zone. However, several authors have observed a trend towards an ω^{-2} spectral shape in the inner surf zone (e.g. Kirby & Kaihatu 1997; Kaihatu *et al.* 2007). Due to the predominance of nonlinear effects over dispersion effects, the waves tend towards a sawtooth shape with a steep front face and a quasi-linear back slope (see figure 1). For idealized sawtooth waves, with discontinuities at wave fronts, the entire energy spectrum follows an ω^{-2} power law. For real sawtooth waves, turbulent motions result in a diffusion-like process at wave fronts. The resulting rounding off of the fronts controls the high-frequency behaviour of the surface elevation spectrum. This is illustrated in figure 2, where two frequency subranges can be identified: an inertial
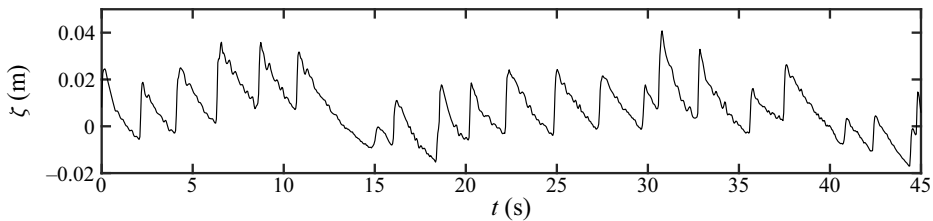
Figure 1. Example of a random sawtooth wave elevation signal in the inner surf zone, where ζ denotes the surface elevation. Laboratory data from van Noorloos (2003), experiment vN03-C3 (see table 1), wave gauge no. 64.
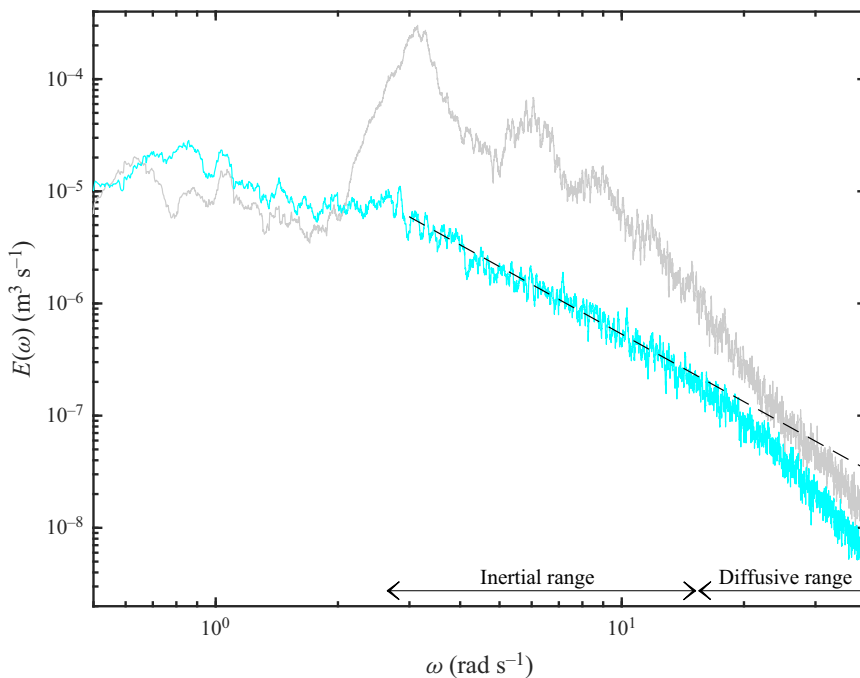

Figure 2. Example of a random sawtooth wave elevation spectrum in the inner surf zone. Laboratory data from van Noorloos (2003), experiment vN03-C3 (see table 1), wave gauge no. 64. The cyan line indicates the sawtooth wave regime; the grey line indicates the beginning of the surf zone; the dashed line shows the ω^{-2} power law.

subrange where the energy spectrum follows an ω^{-2} tendency, and a second subrange where $E(\omega)$ decreases more rapidly with ω. The latter range will be referred to as the diffusive subrange.

In this paper, we analyse the spectral behaviour of random sawtooth waves in the inner surf zone. We show that the energy spectrum, made up of the inertial and diffusive subranges, follows a universal shape. Based on analogies between inner surf zone waves and Burgers turbulence (i.e. 'Burgulence'), we derive a theoretical law for the energy spectrum, and assess its validity from laboratory data. Within this theoretical framework, we analyse the properties of the dissipation spectrum and propose ways to improve its parametrization in stochastic spectral wave models.

2. Physical background

As waves propagate shoreward in decreasing water depth, wave height and nonlinearities increase, leading to wave breaking. After the initiation of breaking (spilling or plunging), a rapid change occurs in the wave shape over a relatively short distance. Shoreward of this region, the wave field reorganizes itself into a succession of relatively stable bore-like waves. This region, referred to by Svendsen, Madsen & Hansen (1978) as the inner surf zone (ISZ), covers a significant part of the surf zone for beaches of regular shape and gentle slope. The ISZ is a self-similar region, where waves are locally depth controlled (Thornton & Guza 1982). Specifically, the ratio of wave height to water depth remains nearly constant. As ISZ waves propagate, they maintain almost the same shape, consisting of a turbulent wave front and a quasi-linear back slope (e.g. Svendsen & Putrevu 1996).

Due to the quasi-linear back slope, the non-hydrostatic effects are very small except at wave fronts (Martins *et al.* 2020). It has been shown that ISZ waves are nearly frequency non-dispersive (e.g. Thornton & Guza (1982), and Martins *et al.* (2021) and their figures 4*g*,*h*). This explains the presence of sawtooth waves (see figure 1), which are a characteristic feature of nonlinear non-dispersive wave phenomena, such as nonlinear acoustic waves (Gurbatov, Rudenko & Saichev 2012). A sawtooth wave (SW) is a coherent structure that results from the competition between dissipation and nonlinearities. Another well-known coherent wave structure, occurring in nonlinear weakly dispersive regimes, is the solitary wave, which results from the balance between dispersion and nonlinearities. However, stable solitary waves occur only in idealized situations, whereas quasi-stable SWs occur in complex natural environments such as the ISZ.

Our study aims to comprehend the spectral behaviour of random SW fields in the ISZ. Our approach is based on the fact that basic characteristics of energy and dissipation spectra within the inertial frequency subrange can be inferred from the SW geometry. For instance, deriving the ω^{-2} power law for the energy spectrum, from a periodic SW signal with discontinuities at wave fronts, is a straightforward process. Furthermore, Kirby & Kaihatu (1997) showed an equipartition of the dissipation over the spectrum (i.e. 'white spectrum') within the inertial subrange. These authors proposed that this phenomenon arises from the fact that dissipation manifests in the space–time domain as a sequence of isolated spike-like processes. To gain a deeper understanding of ISZ energy and dissipation spectra, particularly in the diffusive frequency subrange, we will use the nonlinear shallow-water model, the simplest possible, capable of reproducing the SW shape and localized dissipation at wave fronts. The mathematical simplicity of the model is crucial in order to be able to derive analytical spectral laws.

Bonneton (2007) derived a one-way nonlinear shallow-water model, wherein wave fronts are represented by discontinuities (i.e. shocks) that describe correctly the dynamics of ISZ waves on gently sloping beaches. This model enables a good description of both the nonlinear wave distortion and the energy dissipation. We simplify the model by neglecting bottom variations, resulting in the equation

$$\frac{\partial \zeta}{\partial t} + c_0 \frac{\partial \zeta}{\partial x} + \frac{3}{2} c_0 \frac{\zeta}{h_0} \frac{\partial \zeta}{\partial x} = 0, \tag{2.1}$$

where ζ is the surface elevation, h_0 is the mean water depth, $c_0 = \sqrt{gh_0}$, and g is the acceleration due to gravity. Even though shoaling effects are not considered, wave solutions provided by (2.1) bear a strong resemblance to waves in the ISZ, characterized by their sawtooth shape and localized energy dissipation at wave fronts. However, in essence, this shock-wave approach cannot describe the wave front structure, thus the energy spectrum in the diffusive subrange. In order to overcome this limitation, turbulent

processes can be parametrized by including a diffusivity term $\nu_t(\partial^2\zeta/\partial x^2)$ on the right-hand side of (2.1), with ν_t a turbulent diffusion coefficient.

In the frame of reference moving at velocity c_0, and making the change of variable

$$v = \frac{3c_0}{2h_0}\,\zeta, \tag{2.2}$$

(2.1) can be rewritten as

$$\frac{\partial v}{\partial t} + v\,\frac{\partial v}{\partial x} = \nu_t\,\frac{\partial^2 v}{\partial x^2}. \tag{2.3}$$

Throughout this paper, we will use this idealized one-way nonlinear shallow-water model as a toy model to infer the SW spectral behaviour.

3. Burgers turbulence

3.1. *Burgers model*

To further simplify our wave problem, we consider in § 3 that the diffusion coefficient ν_t is constant ($\nu_t = \nu$). Equation (2.3) is then the well-known Burgers equation. It was introduced originally as a simple one-dimensional model to contribute to the study of turbulence (Burgers 1948). A synthesis on Burgers turbulence, also known as Burgulence, is presented in Frisch & Bec (2002).

In this subsection, we consider freely decaying random waves $v(x, t)$ that are statistically homogeneous in space, with zero mean. The equation for the mean energy $E_v = \langle v^2 \rangle$ is

$$\frac{\partial E_v}{\partial t} = -D_v, \tag{3.1}$$

where $D_v = 2\nu\,\langle(\partial v/\partial x)^2\rangle$ is the energy dissipation, and $\langle\,\cdot\,\rangle$ is the spatial mean.

A striking feature of Burgers solutions is the formation of shocks. Due to the nonlinear term, negative v slopes are steepened in time until they build up into diffusive shocks, where nonlinear and diffusive effects are balanced. For initial random conditions, the wave field tends towards an irregular sawtooth profile, quite similar to that of SWs in the ISZ (figure 1).

Two main characteristic scales are involved in the SW regime: λ_m is the mean distance between adjacent wave fronts, and V_c is the characteristic scale of velocity jumps at wave fronts. The wave field is then controlled by two length scales: a macroscopic one, λ_m, and a small one, the average shock thickness $\delta \sim \nu/V_c$. Consequently, the problem is governed by one dimensionless parameter, the Burgers-type Reynolds number $R_B = V_c\lambda_m/\nu$. It is well established that for wavenumbers ranging from $k_m = 2\pi/\lambda_m$ to the diffusive wavenumber k_ν ($k_\nu \sim \delta^{-1}$), the Burgers energy spectrum follows a k^{-2} power law (e.g. Tatsumi 1969). This k^{-2} subrange is followed at high k by a diffusive subrange where the energy decreases more rapidly.

We will see later that ISZ waves are characterized by moderate Reynolds numbers of approximately a few hundreds ($R_B \sim 100$–500). In this section, we analyse the spectral characteristics of Burgers waves for this R_B range. It should be noted that most studies on Burgulence, unlike ours, focus on regimes with very high R_B. When referring to an ISZ wave, R_B must be distinguished from the classical Reynolds number based on the kinematic viscosity. Before analysing random waves, we start by studying the nonlinear dynamics of periodic SWs. This idealized case is very useful, first for understanding basic

nonlinear and dissipative processes in the spectral space, and second by serving as a basis for the development of a random SW theory.

3.2. *Periodic sawtooth waves*

In the non-diffusive case ($\nu = 0$), the derivation of the periodic SW Burgers solution, $v_i(x, t)$, from the method of characteristics is straightforward and gives

$$v_i = \frac{V_J(t)}{2} \left(\frac{2x}{\lambda} - \text{sgn}(x) \right), \quad x \in \left[-\frac{\lambda}{2}, \frac{\lambda}{2} \right], \tag{3.2}$$

where λ is the wavelength, $V_J(t) = V_0/(1 + V_0 t/\lambda)$ is the velocity jump across the inviscid shock (located in $x = 0$), and V_0 is the velocity jump at $t = 0$. Khokhlov derived an exact SW solution of the diffusive Burgers equation (see Gurbatov *et al.* (2012)):

$$v = \frac{V_J(t)}{2} \left(\frac{2x}{\lambda} - \tanh \frac{V_J(t)\, x}{4\nu} \right). \tag{3.3}$$

This solution is not periodic, but for large Reynolds numbers it becomes quasi-periodic between $x = -\lambda/2$ and $x = \lambda/2$, with a diffusive front located in $x = 0$. The dimensionless velocity jump $\delta v_b = \left(v(\lambda/2^-) - v(\lambda/2^+) \right)/V_J = 1 - \tanh(R_B/8)$ is an exponentially decreasing function of R_B. For the R_B values that concern us, we can consider the solution (3.3) as periodic due to the small value of δv_b ($\delta v_b < 10^{-11}$).

For large R_B, an approximate relationship of total dissipation D_ν can be derived. Using (3.3) and retaining only the leading terms in an expansion in powers of R_B gives

$$\left\langle \left(\frac{\partial v}{\partial x} \right)^2 \right\rangle = \frac{1}{12} \frac{V_J^3}{\nu \lambda} \tag{3.4}$$

and then

$$D_\nu = \frac{1}{6} \frac{V_J^3}{\lambda}. \tag{3.5}$$

This shows that for R_B of interest, the total dissipation is virtually independent of ν.

One of the main objectives of this paper is to analyse the spectral behaviour of SWs. In the case of periodic waves, it is possible to derive an expression for the energy spectral density from the Khokhlov solution (3.3) (see § A.1 in the supplementary material available at https://doi.org/10.1017/jfm.2023.878). This expression is written as

$$\mathcal{E}_{v_n} = 2\nu^2 k_p^2 \, \text{csch}^2 \left(\frac{k_n}{k_\nu} \right), \tag{3.6}$$

where $\mathcal{E}_{v_n} = v_n^2/2$ is the energy spectral density, v_n is the nth Fourier coefficient of v, $k_p = 2\pi/\lambda$, $k_n = n k_p$ and $k_\nu = V_J/2\pi\nu$. For $k_n/k_\nu \ll 1$, $\mathcal{E}_{v_n}$ follows a k_n^{-2} power law:

$$\mathcal{E}_{v_n} = \frac{2V_J^2}{\lambda^2} k_n^{-2}. \tag{3.7}$$

This last relation is also the exact energy spectral density of the non-diffusive SW solution (3.2). For $k_n/k_\nu \gg 1$, $\mathcal{E}_{v_n}$ decreases exponentially with k_n. In the following, the inertial and diffusive subranges will be defined respectively as $k \in [k_p, k_\nu]$ and $k \in [k_\nu, \infty]$.

977 A48-6

The dimensionless width of the inertial subrange, $(k_v - k_p)/k_p$, increases linearly with R_B, since $k_v/k_p = R_B/(4\pi^2)$.

Substituting the Fourier series representation of v into the Burgers equation, we obtain the spectral energy equation

$$\frac{\mathrm{d}}{\mathrm{d}t}\mathcal{E}_{v_n} + \mathcal{T}_{v_n} = -\mathcal{D}_{v_n}, \tag{3.8}$$

where $\mathcal{D}_{v_n} = 2\nu k_n^2 \mathcal{E}_{v_n}$ is the dissipation spectrum, and $\mathcal{T}_{v_n}$ the nonlinear transfer function. This last can be expressed as

$$\mathcal{T}_{v_n} = \frac{k_n}{4} \, v_n \sum_{m=1}^{n-1} v_m v_{n-m} - \frac{k_n}{2} \, v_n \sum_{m=1}^{\infty} v_m v_{n+m}, \tag{3.9}$$

where the first term on the right-hand side represents the triad sum interactions of components $(m, n - m)$, and the second term represents the triad difference interactions of components $(m, n + m)$.

In order to better understand the spectral behaviour of dissipation and nonlinear interactions, we analyse the different terms in (3.8). Substituting (3.6) into $\mathcal{D}_{v_n} = 2\nu k_n^2 \mathcal{E}_{v_n}$, we get the dissipation spectrum

$$\mathcal{D}_{v_n} = 4\nu^3 k_p^2 k_n^2 \operatorname{csch}^2\left(\frac{k_n}{k_v}\right), \tag{3.10}$$

which is a decreasing function of k_n. For $k_n/k_v \ll 1$, the dissipation spectrum given by

$$\mathcal{D}_{v_n} = \frac{4\nu V_J^2}{\lambda^2} \tag{3.11}$$

is constant. The nonlinear transfer function can be obtained from $\mathcal{T}_{v_n} = -((\mathrm{d}\mathcal{E}_{v_n}/\mathrm{d}t) + \mathcal{D}_{v_n})$, which results in

$$\mathcal{T}_{v_n} = -2\nu k_n \left(k_n - k_p \coth\left(\frac{k_n}{k_v}\right)\right) \mathcal{E}_{v_n}. \tag{3.12}$$

Figure 3 illustrates the contribution of each term in the spectral energy equation (3.8). We consider two SW fields with the same V_J and λ but two contrasting Reynolds numbers $R_B = 100$ and $R_B = 500$ (respectively, minimum and maximum R_B values observed in the ISZ experiments discussed in § 5). This means that we analyse two similar wave fields that have almost the same shape except at the wave front. Figure 3 shows that the temporal rate of change of the energy spectrum, $\mathrm{d}\mathcal{E}_{v_n}/\mathrm{d}t$, is virtually independent of R_B. This temporal rate of change follows the approximate relation for large R_B

$$\frac{\mathrm{d}}{\mathrm{d}t}\mathcal{E}_{v_n} = -\frac{D_v}{E_v} \, \mathcal{E}_{v_n}, \tag{3.13}$$

where $E_v = V_J^2/12$, and D_v and $\mathcal{E}_{v_n}$ are given by (3.5) and (3.7), respectively. This explains why the energy spectrum shape is practically preserved as SWs evolve with time. Contrary to $\mathrm{d}\mathcal{E}_{v_n}/\mathrm{d}t$, the dissipation spectrum $\mathcal{D}_{v_n}$ and the nonlinear transfer function $\mathcal{T}_{v_n}$ are strongly dependent on R_B. For the highest R_B ($R_B = 500$), figure 3 shows that $\mathcal{T}_{v_1} \gg \mathcal{D}_{v_1}$, meaning that for the first wave mode (the most energetic), the rate of change of the energy spectrum is controlled mainly by energy transfer to higher wavenumbers. By contrast, for
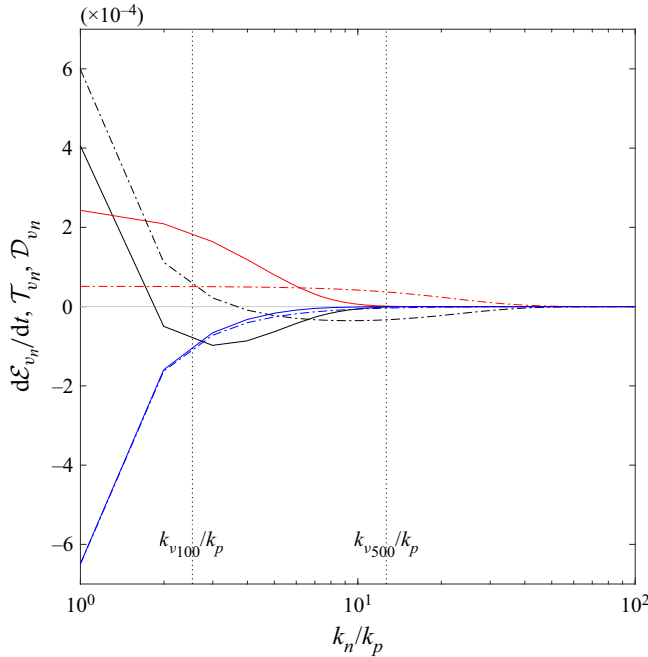
Figure 3. Dissipation spectrum and nonlinear transfer function for two SW solutions with the same V_J and λ but distinct Reynolds numbers: $R_B = 100$ (continuous lines) and $R_B = 500$ (dash-dotted lines). Red lines indicate $\mathcal{D}_{v_n}$ (3.10); black lines indicate $\mathcal{T}_{v_n}$ (3.12); blue lines indicate $\mathrm{d}\mathcal{E}_{v_n}/\mathrm{d}t = -(\mathcal{D}_{v_n} + \mathcal{T}_{v_n})$; dotted lines indicate positions of k_v/k_p. For the sake of clarity, we use lines (continuous or dash-dotted) to represent the discrete spectra.

the lower R_B ($R_B = 100$), $\mathcal{T}_{v_1}$ is of the same order of magnitude as $\mathcal{D}_{v_1}$, thus the nonlinear energy transfer and the energy dissipation contribute nearly equally to the energy decrease with time. We can see in figure 3 that $\mathcal{D}_{v_n}$ is nearly constant in the inertial subrange following (3.11), and decreases strongly in the high wavenumber tail of the spectrum (i.e. the diffusive subrange). In the diffusive subrange, $|\mathrm{d}\mathcal{E}_{v_n}/\mathrm{d}t|$ is much smaller than $\mathcal{D}_{v_n}$ and $|\mathcal{T}_{v_n}|$. This means that for high wavenumbers, there is a balance between the dissipation and the nonlinear energy transfer from low wavenumbers. This result seems in line with surf zone field observations by Herbers, Russnogle & Elgar (2000).

To summarize this part, $\mathrm{d}\mathcal{E}_{v_n}/\mathrm{d}t$ is governed primarily not by nonlinear interactions, even at low k_n, but rather by the competition between $\mathcal{D}_{v_n}$ and $\mathcal{T}_{v_n}$, which are both strongly dependent on diffusion processes at wave fronts. This conclusion, obtained for periodic SW, cannot be applied directly to ISZ random SW, which are a more complex phenomenon. However, these results may give ideas on how diffusive processes could affect the dissipation and the nonlinear interactions of ISZ SWs.

3.3. *Random sawtooth waves*

We now consider freely decaying random solutions $v(x, t)$ that are statistically homogeneous in space with zero mean. The power spectral density $\Phi(k, t)$ is the Fourier transform of the autocorrelation function $R(r)$:

$$\Phi(k, t) = \frac{1}{2\pi} \int_{-\infty}^{\infty} R(r) \exp(-\mathrm{i}kr) \, \mathrm{d}r, \tag{3.14}$$

where $R(r, t) = \langle v(x, t)\, v(x + r, t) \rangle$. As $\Phi(k, t)$ is an even function of k, we limit our analysis to $k \geq 0$, and denote $E_v(k, t) = 2\Phi(k, t)$ the power spectral density function. With this notation, the total energy $E_v = \langle v^2 \rangle = \int_{-\infty}^{\infty} \Phi(k)\, dk$ can be expressed as

$$E_v = \int_0^{\infty} E_v(k)\, dk. \tag{3.15}$$

Throughout the paper, E_v will denote the energy spectrum. In the spectral space, the energy equation is given by

$$\frac{\partial E_v}{\partial t} + T_v = -D_v, \tag{3.16}$$

where $D_v(k, t) = 2\nu k^2 E_v(k, t)$ is the spectral energy dissipation, $T_v(k, t) = -k \int_{-\infty}^{\infty} \text{Im}(B)\, dl$ is the nonlinear transfer term, and $B(k, l, t)$ is the bispectrum.

Saffman (1968) assumed that the periodic solution (3.3) reproduces the qualitative features of the small-scale behaviour of random SWs. From this hypothesis, he derived an expression for the energy spectrum, which is consistent with (3.6) obtained for the energy density function of periodic SWs. The equation for the energy spectrum is given by

$$E_v(k, t) = 2\nu^2\, k_m(t)\, \text{csch}^2\left(\frac{k}{k_\nu(t)}\right), \quad k \in [k_m, \infty], \tag{3.17}$$

where $k_\nu = V_c/2\pi\nu$ is the diffusive wavenumber, V_c is the characteristic scale of v-jumps at wave fronts, $k_m = 2\pi/\lambda_m$, and λ_m is the mean distance between adjacent wave fronts. The Reynolds number $R_B = V_c\lambda_m/\nu$ can be expressed as $R_B = 4\pi^2(k_\nu/k_m)$. The derivation of Saffman (1968) equation is presented in § A.2 of the supplementary material, where we have both clarified the definition of the characteristic horizontal length scale and corrected an error in the hyperbolic cosecant term. This theory applies to short waves (i.e. SW scale) and not to wavenumbers smaller than approximately k_m. For the sake of clarity, explicit reference to time has been omitted in the following equations.

For periodic SWs, the definition of the characteristic scale of v-jumps, V_J, is straightforward. It is the non-diffusive v-jump associated with the diffusive SW solution (3.3). The characteristic v-scale, V_c, in random SW fields is not explicit. It can be obtained implicitly from $\tilde{E}_v = \int_{k_m}^{\infty} E_v(k)\, dk$, the total energy over the wavenumber range $[k_m, \infty]$. By integrating (3.17) from k_m to ∞, we obtain

$$\tilde{E}_v = 2\nu^2 k_m k_\nu \left(\coth(k_m/k_\nu) - 1\right). \tag{3.18}$$

Given k_m and $\tilde{E}_v = \int_{k_m}^{\infty} E_v(k)\, dk$, the implicit equation (3.18) yields k_ν and then V_c. Thus, for a given random SW field characterized by k_m and $\tilde{E}_v$, (3.17) can predict the energy spectrum.

For $k \ll k_\nu$, $E_v(k)$ follows a k^{-2} power law independent of the diffusion coefficient ν,

$$E_v(k) = \left(\frac{k_m V_c^2}{2\pi^2}\right) k^{-2}, \tag{3.19}$$

and for $k \gg k_\nu$, $E(k)$ decreases exponentially with k,

$$E_v(k) = 8\nu^2 k_m \exp\left(-2\frac{k}{k_\nu}\right). \tag{3.20}$$

The dissipation spectrum $D_v(k, t) = 2\nu k^2 E_v(k, t)$ is given by

$$D_v(k) = 4\nu^3 k_m k^2 \operatorname{csch}^2\left(\frac{k}{k_v}\right), \quad k \in [k_m, \infty], \tag{3.21}$$

and its asymptotic form for small k is

$$D_v(k) = \frac{\nu k_m V_c^2}{\pi^2}. \tag{3.22}$$

It is worth noting that at large scale, the dissipation spectrum is constant, which means that there is equipartition of dissipation over the spectrum. The exponential decay of $E_v(k)$ at large wavenumbers guarantees that the k-integrated dissipation, $\tilde{D}_v = \int_{k_m}^{\infty} D_v(k) \, dk$, is finite. To my knowledge, the theoretical model (3.17) has never been validated. In order to test the validity of this model, we have computed numerically random SW solutions of the Burgers equation. It is solved with a spectral method where aliasing is avoided by using the so-called 3/2 rule. The initial random v-field, $v_0(x) = v(x, 0)$, is specified in the Fourier space by the energy spectrum

$$E_0(k) = E_0 \frac{k}{k_p} \exp\left(-\frac{1}{2}\left((k/k_p)^2 - 1\right)\right), \tag{3.23}$$

where $k_p = 2\pi/\lambda_p$ is the peak wavenumber, and E_0 is the energy at k_p. The phase of each wavenumber is assigned a random value in the range $[0, 2\pi]$. The length of the domain covers $2^8 \lambda_p$ and is discretized over 2^{16} grid points. The computed spectra $E_v(k, t)$ are estimated by an ensemble average over 1000 realizations.

Figure 4 illustrates the time evolution of the energy spectrum. The cascade of energy towards high wavenumbers, due to nonlinear triad interactions, leads to a rapid transition to an established SW regime. In this regime, the theoretical law (3.17) gives a very good description of the numerically computed spectra. The inertial and diffusive subranges are well represented by the k^{-2} power law (3.19) and by an exponential decrease (3.20), respectively. However, (3.17) tends to slightly underestimate the numerically computed spectrum at large wavenumbers ($k > 20k_p$), whatever the numerical resolution. Contrary to the monochromatic case, the wavenumber k_m is not constant and decreases with time due to shock merging. Consequently, the inertial subrange width, and thus the Reynolds number, decreases at a slower rate than in the monochromatic case. The time evolution of the dissipation spectrum is shown in figure 5. We observe very good agreement between the theoretical law (3.21) and the numerically computed dissipation spectra. In the inertial subrange, the dissipation is constant, in agreement with the non-diffusive SW theory (3.22). Then, in the diffusive subrange, the dissipation decreases exponentially. It is worth noting that for Burgers turbulence, the dissipation occurs mainly in the inertial subrange, unlike the classical hydrodynamic turbulence where dissipation occurs at smaller scale.

4. Analytical energy spectrum for ISZ waves

The above results for the Burgers equation apply directly to the one-way shallow-water equation (2.1). Therefore, we can describe the spectral behaviour of irregular SWs, statistically homogeneous in space, propagating freely in a constant water depth at celerity $c_0 = \sqrt{gh_0}$. However, ISZ waves are not statistically homogeneous in space, since they are forced at the offshore limit of the ISZ and propagate over a varying mean
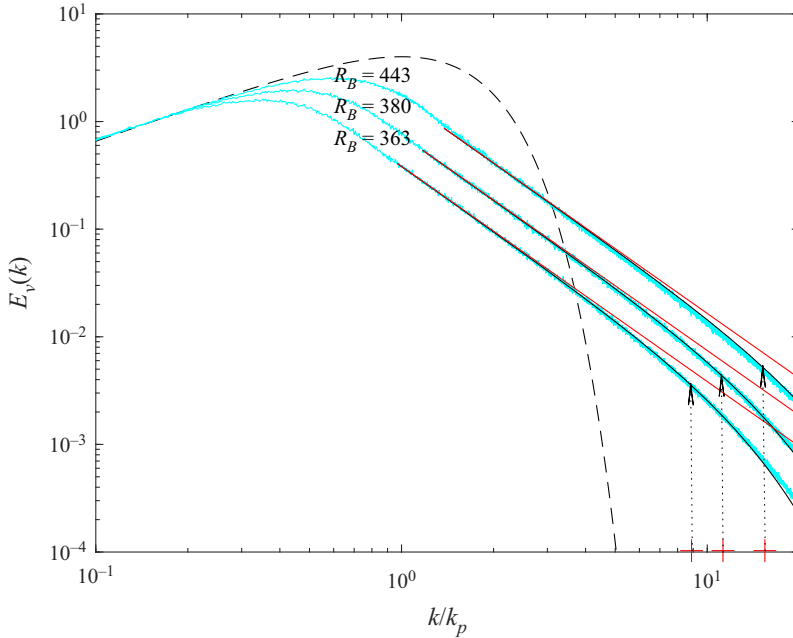
Figure 4. Time evolution of the power spectral density for an initial condition given by (3.23). Dashed line indicates initial condition; cyan lines indicate numerical simulations at dimensionless times $t/t_* = 1.45, 2.90, 4.85$ (corresponding to Reynolds numbers $R_B = 443, 380, 363$), where $t_* = 1/(k_p\sqrt{E_{T_0}})$; black line indicates theoretical model (3.17) starting from $k = k_m$; red line indicates k^{-2} power law (3.19); red plus symbol indicates position of k_ν/k_p. The length of the domain covers $2^8\lambda_p$ and is discretized over 2^{16} grid points. Spectra have been averaged over 1000 realizations.
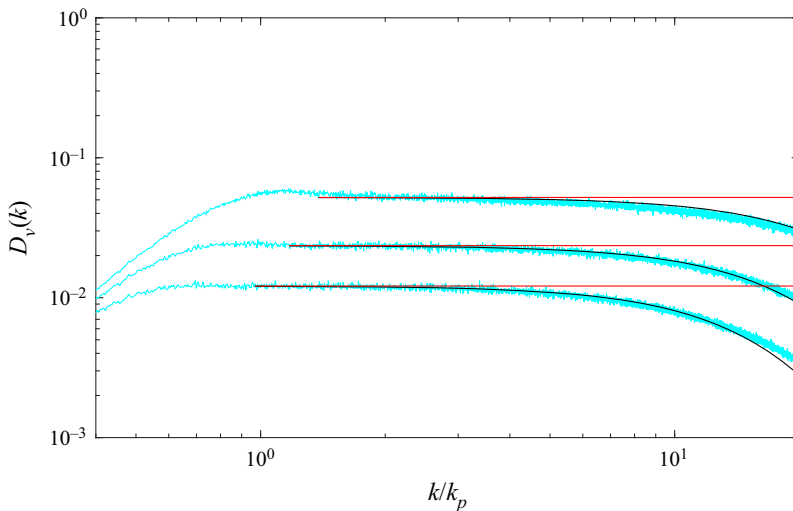
Figure 5. Time evolution of the dissipation spectrum for an initial condition given by (3.23). Cyan lines indicate numerical simulations at dimensionless times $t/t_* = 1.45, 2.90, 4.85$ (corresponding to Reynolds numbers $R_B = 443, 380, 363$), where $t_* = 1/k_p\sqrt{E_{T_0}}$; black lines indicate the theoretical model (3.21) starting from $k = k_m$; red lines indicate (3.22). The length of the domain covers $2^8\lambda_p$ and is discretized over 2^{16} grid points. Spectra have been averaged over 1000 realizations.

water depth $h_0(x)$. Subsequently, we will make the strong assumption that for slowly varying bathymetry, the shape of the energy spectrum in the wavenumber space can be estimated using the corrected Saffman equation (3.17). It should also be noted that unlike Burgers-like waves, ISZ waves are asymmetric with respect to the mean water level (i.e. are skewed). In fact, their back slope is not linear but convex. However, the curvature is small enough not to affect the k^{-2} tendency of the energy spectrum in the inertial subrange.

Laboratory and field experiments (Thornton & Guza 1982; Elgar & Guza 1985*a*; Martins *et al.* 2021) showed that in the ISZ, most wave components of the spectrum are bounded and propagate to the same celerity c_m close to the non-dispersive celerity in shallow water, c_0. From laboratory experiments analysed in § 5, we have verified that this spectral behaviour also holds for high frequencies in the diffusive subrange. The ISZ celerity can be estimated by the relation $c_m = \alpha_c c_0$, where $\alpha_c \simeq 1.1$–1.2 (Tissier *et al.* 2011; Martins *et al.* 2021). Using the dispersion relation $\omega = c_m k$, we can estimate the energy spectrum in the frequency domain, $E_v(\omega)$, from that in the wavenumber domain. The spectrum $E_v(\omega)$ can then be written

$$E_v(\omega) = \frac{2v_c^2 \omega_m}{c_0^2} \operatorname{csch}^2 \left(\frac{\omega}{\omega_v} \right), \quad \omega \in [\omega_m, \infty], \tag{4.1}$$

where $v_c(x)$ is a characteristic turbulent diffusion coefficient that varies in space, and $\omega_m = 2\pi/T_m$, with T_m the mean time between adjacent wave fronts, and ω_v the diffusive angular frequency. For the sake of simplicity, the empirical coefficient α_c, which is close to 1, does not appear in the spectrum equation. It has been integrated into the diffusion coefficient, resulting in the actual diffusion coefficient being equal to $\alpha_c v_c$.

Making the change of variable (2.2) to come back to the physical scale ζ, we obtain the following expression for the energy spectrum in the frequency domain $E(\omega)$:

$$E(\omega) = \frac{8}{9} \frac{v_c^2}{g} \omega_m \operatorname{csch}^2 \left(\frac{\omega}{\omega_v} \right), \quad \omega \in [\omega_m, \infty], \tag{4.2}$$

where $\omega_v = (3/4\pi)(gH_c/v_c)$, and H_c is the characteristic scale of elevation jumps at wave fronts. This scale is related to the characteristic scale of v-jumps V_c by $H_c = \frac{2}{3}(h_0/c_0)V_c$. Contrary to the Burgers case, the turbulent diffusion coefficient v_c is here an unknown of the problem. The total wave energy is defined by $E = \overline{g\zeta^2} = \int_0^\infty E(\omega) \, d\omega$, where $\overline{(\cdot)}$ is the time average operator. For $\omega \ll \omega_v$, $E(\omega)$ follows an ω^{-2} power law,

$$E(\omega) = \left(\frac{g\omega_m H_c^2}{2\pi^2} \right) \omega^{-2}, \tag{4.3}$$

and for $\omega \gg \omega_v$, it decreases exponentially with ω,

$$E(\omega) = \frac{32}{9} \frac{v_c^2}{g} \omega_m \exp \left(-2 \frac{\omega}{\omega_v} \right). \tag{4.4}$$

The energy spectrum can be expressed in a dimensionless form as

$$\frac{E(\omega)}{E_m} = \left(\frac{\omega_m}{\omega_v} \right)^2 \operatorname{csch}^2 \left(\frac{\omega_m}{\omega_v} \frac{\omega}{\omega_m} \right), \tag{4.5}$$

where $E_m = gH_c^2/2\pi^2\omega_m$. The shape of the energy spectrum is thus controlled entirely by the dimensionless number ω_m/ω_v, or equivalently by the Reynolds number

977 A48-12

	H_i (cm)	h_i (cm)	f_p (Hz)	Spectrum	γ	s	f_s (Hz)
vN03-C3	$H_{m0} = 10$	70	0.5	JONSWAP	3.3	1/35	25
vN03-D3	$H_{m0} = 10$	70	0.65	JONSWAP	3.3	1/35	25
MK93	$H_{rms} = 4$	47	0.6	Pierson–Moskowitz	1	1/20	25
BK94-7	$H_{rms} = 7$	44	0.5	TMA	3.3	1/35	25
BK94-8	$H_{rms} = 8$	44	0.225	TMA	3.3	1/35	25
BK94-9	$H_{rms} = 9$	44	0.225	TMA	3.3	1/35	25

Table 1. Experimental parameters: H_i, incident wave height; h_i, water depth; f_p, peak frequency; γ, peak-enhancement factor; s, bottom slope; f_s, sampling rate.

$R_B = 4\pi^2(\omega_\nu/\omega_m) = \frac{3}{2}(gH_cT_m/\nu_c)$. In the following, the inertial and diffusive subranges will be defined respectively as $\omega \in [\omega_m, \omega_\nu]$ and $\omega \in [\omega_\nu, \infty]$. The dimensionless width of the inertial subrange, $(\omega_\nu - \omega_m)/\omega_m$, increases linearly with R_B.

The nonlinearities of shallow-water waves are usually characterized by the dimensionless parameter $\epsilon = H_c/2/h_0$, which quantifies the relative importance of nonlinearities over the linear advection. For waves propagating in the ISZ over a regular low slope bottom, the nonlinearity parameter ϵ changes very little and has a value of approximately 0.2–0.3 (e.g. Svendsen *et al.* 1978; Thornton & Guza 1982). Reynolds number R_B, on the other hand, quantifies the relative importance of nonlinearities with respect to turbulent diffusion. We will see in the next section that this second nonlinearity parameter, contrary to ϵ, evolves strongly as waves propagate in the ISZ.

5. Application to laboratory experiments

5.1. *Description of datasets*

The theoretical approach developed above is now evaluated against laboratory experiments on random wave propagation and breaking on a uniform slope. Six laboratory datasets are used: one from Mase & Kirby (1993) (hereafter MK93), three from Bowen & Kirby (1994) (BK94), and two from van Noorloos (2003) (vN03). These experiments cover a large variety of incident random wave conditions in terms of frequency peak f_p, wave height H_i, and spectral shape. The random waves were generated at the wave paddle using random realizations of analytical single-peaked spectra. Mase & Kirby (1993) chose a Pierson–Moskowitz spectrum that can be seen in figure 6(*c*) (blue line). van Noorloos (2003) used a JONSWAP spectrum with a peak-enhancement factor $\gamma = 3.3$, which provides a much sharper frequency peak than that of the Pierson–Moskowitz spectrum (see blue lines in figures 6*a*,*b*). Bowen & Kirby (1994) chose a TMA spectrum, which is an extension of the JONSWAP spectrum describing waves in finite depth. In shallow water, the TMA spectrum follows an ω^{-3} power law, which results in a broader spectrum than the JONSWAP spectrum (see blue lines in figures 6*d*–*f*). In all these experiments, the wave gauges are sampled at frequency 25 Hz. For our spectral analysis, we will consider frequency lower than half the Nyquist frequency, i.e. $\omega < \omega_{max} = 40\,\text{rad}\,\text{s}^{-1}$. The smallest wavelength, associated with ω_{max}, is approximately 10 cm, a scale much larger than capillary wave scales. The experimental parameters of the six datasets are given in table 1.

As incoming waves shoal, energy is transferred from the most energetic portion of the energy spectrum (around the spectral peak) to both higher and lower frequencies
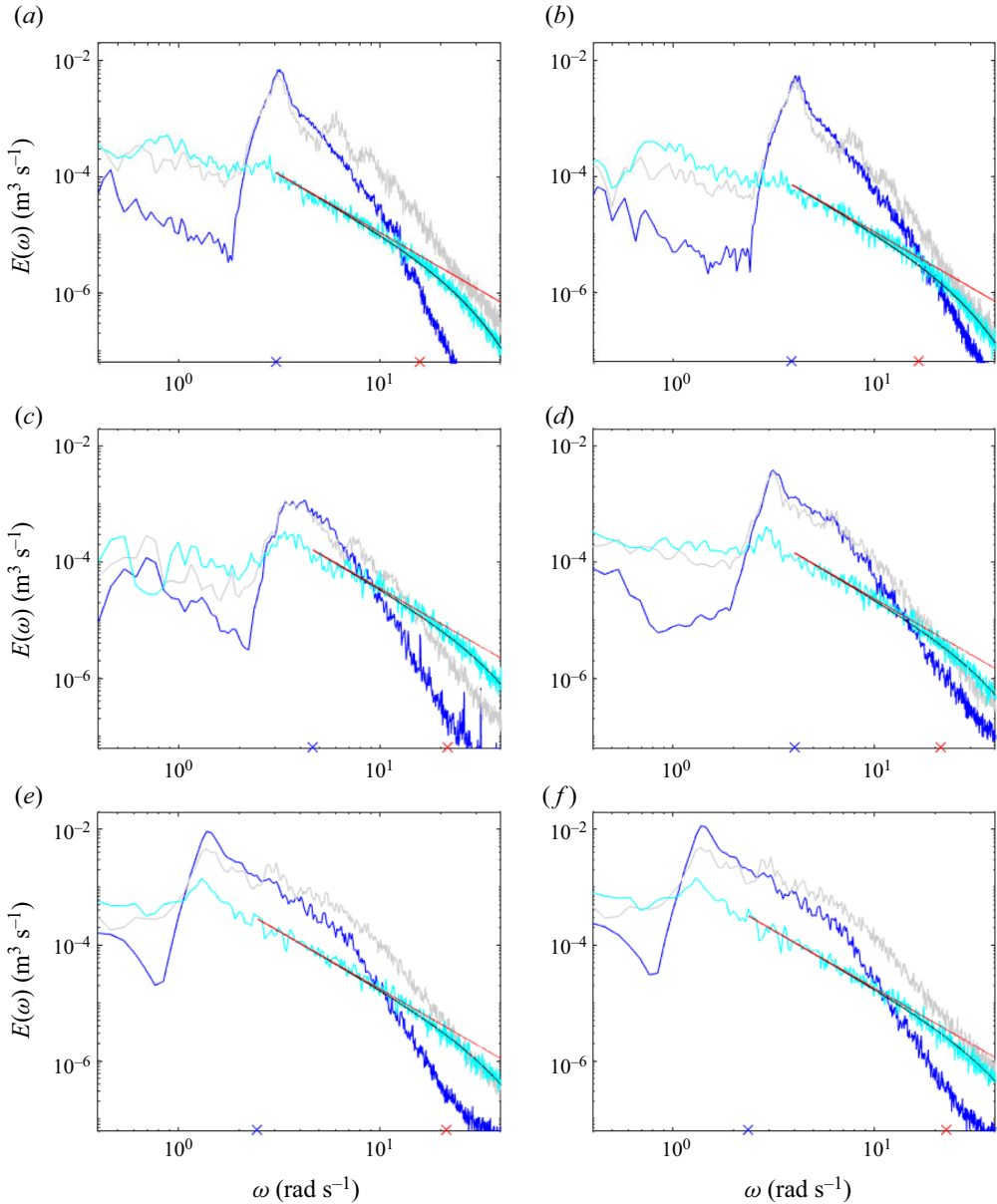
Figure 6. Energy spectra for (*a*) vN03-C3, (*b*) vN03-D3, (*c*) MK93, (*d*) BK94-7, (*e*) BK94-8, and (*f*) BK94-9. Blue line indicates incident wave spectrum; grey line indicates spectrum at the breaking point; cyan line indicates ISZ spectrum in a mean water depth $h_0 = 5.5$ cm; black line indicates (4.2); red line indicates (4.3). Blue cross indicates position of ω_m; red cross indicates position of ω_v.

(figure 6). At the breaking point, the spectrum shape depends strongly on the incident wave spectrum. For instance, narrow-band spectra (see figures 6*a*,*b*) develop harmonic peaks of the fundamental frequency and infragravity waves (i.e. waves with frequency lower than approximately $0.5f_p$) that are both significantly larger than those associated with broad-band incident wave spectra. By contrast, in the ISZ, the high-frequency part ($\omega > \omega_m$) of the wave spectrum always has a regular shape with an ω^{-2} tendency in

977 A48-14

the inertial subrange, whatever the incident wave conditions. The ω^{-2} tendency of ISZ wave spectra was already noticed by Kirby & Kaihatu (1997). While the shape of the high-frequency part of the ISZ spectrum is almost independent of the incident wave conditions, this is not the case for the frequency bounds of the inertial subrange. The lower bound ω_m is an increasing function of the frequency peak of the incident wave spectrum ω_p. Moreover, the time evolution of ω_m is controlled in the surf zone by the wave front merging phenomenon. Tissier, Bonneton & Ruessink (2017) showed that this phenomenon is favoured by the presence of infragravity waves whose intensity depends on incident wave conditions.

5.2. *Assessment of the analytical wave energy spectrum*

To apply the theoretical spectrum (4.2) to a laboratory dataset, it is necessary to know the three parameters ω_m, ω_ν and ν_c. The parameter ν_c can be substituted by the energy $\tilde{E} = \int_{\omega_m}^{\infty} E(\omega)\,\mathrm{d}\omega$ using the equation

$$\tilde{E} = \frac{8}{9}\frac{\nu_c^2}{g}\,\omega_m \omega_\nu \left(\coth(\omega_m/\omega_\nu) - 1\right). \tag{5.1}$$

For each dataset, the mean time T_m between adjacent wave fronts is obtained from a wave-by-wave analysis that identifies each SW front. The energy $\tilde{E}$ is then calculated by integrating the experimental energy spectrum from $\omega_m = 2\pi/T_m$ to the Nyquist frequency. The diffusive frequency ω_ν is an unknown of the problem. To evaluate this frequency, we use a nonlinear least squares method to fit the measured spectrum with the theoretical one, rewritten in the form

$$\frac{E(\omega)}{\tilde{E}} = \frac{\mathrm{csch}^2\left(\dfrac{\omega}{\omega_\nu}\right)}{\omega_\nu\left(\coth(\omega_m/\omega_\nu) - 1\right)}. \tag{5.2}$$

For the whole dataset, the diffusive frequency ω_ν ranges from 14.5 to 25.8 rad s^{-1} (i.e. $f_\nu = \omega_\nu/(2\pi) \in [2.3, 4.1]$ Hz). Knowing ω_ν, we obtain finally ν_c from (5.1).

Figure 6 shows ISZ spectra measured in 5 cm water depth for the six contrasting datasets (see table 1). Whatever the random wave forcing, the ISZ spectral shape is well described by the theoretical spectrum (4.2). The ω^{-2} tendency is identifiable on all measured spectra. However, this tendency is, of course, less marked for a small inertial subrange, i.e. small R_B (e.g. see figure 6*b*) than for large R_B (see figure 6*f*).

We are now interested in the evolution of the ISZ wave spectrum as waves propagate shoreward in decreasing water depth. The measured wave spectra are very well described by (4.2) irrespective of the dataset and the water depth (see figures 7 and 8, and in the supplementary material, figures 3–6). As illustrated in figure 9, by scaling measured wave spectra by $E_a = 8\nu_c^2\omega_m/9g$, data collapse on a single curve given by the dimensionless universal spectrum equation

$$\frac{E}{E_a} = \mathrm{csch}^2\left(\frac{\omega}{\omega_\nu}\right). \tag{5.3}$$

Spectra differ only in their dimensionless inertial range width $(\omega_\nu - \omega_m)/\omega_\nu$. We focus our analysis on two contrasting datasets: BK94-9 (figure 7) and vN03-C3 (figure 8). In both cases, we observe a decrease in ω_m as waves propagate (i.e. h_0 decreases), which is due to the bore merging phenomenon. This decrease is much stronger for vN03-C3 (from 3.53
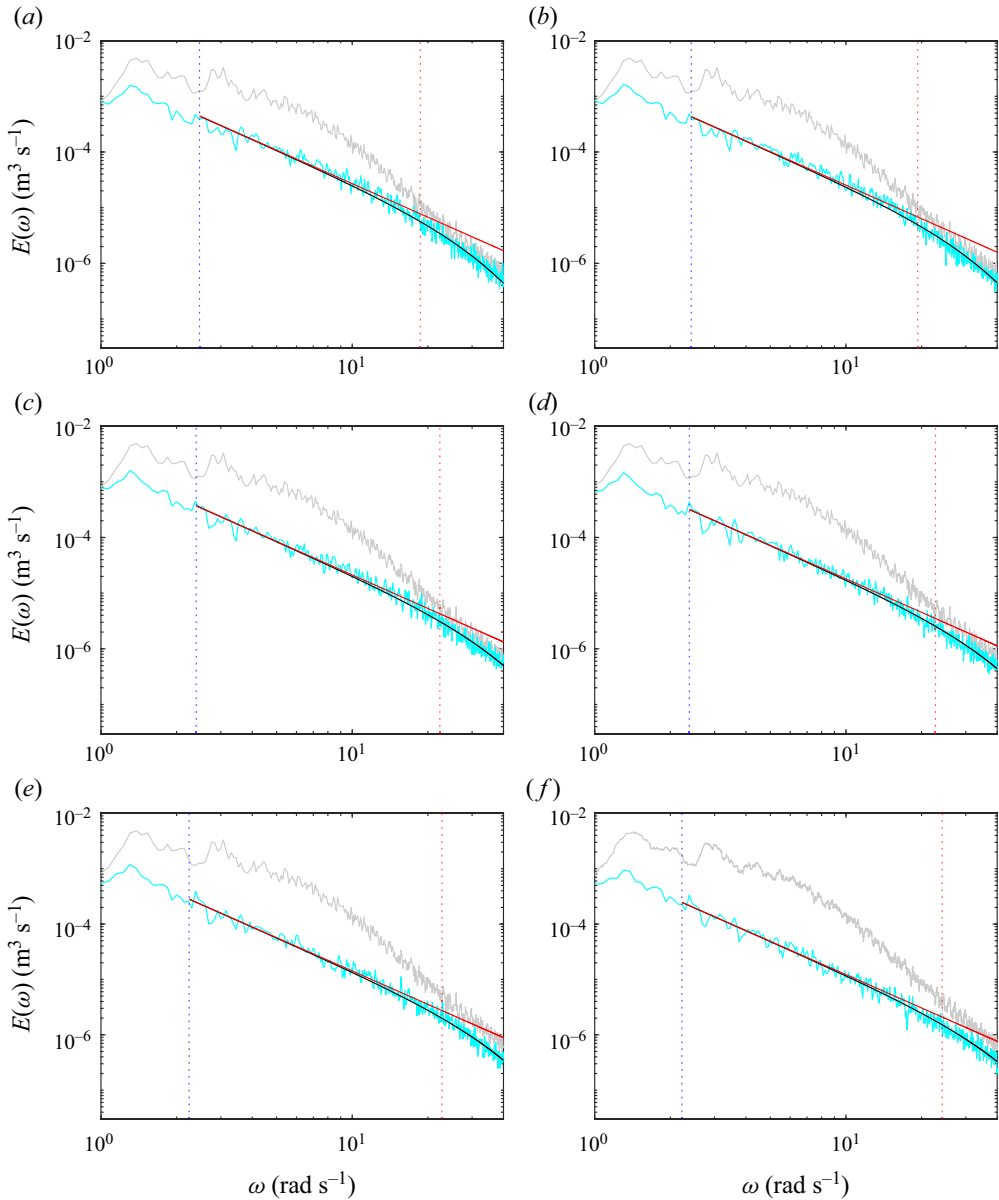
Figure 7. Energy spectra at different locations in the ISZ for the BK94-9 experiment: (*a*) $x = 24.50$ m, $h_0 = 7.6$ cm; (*b*) $x = 24.72$ m, $h_0 = 6.8$ cm; (*c*) $x = 24.97$ m, $h_0 = 6.2$ cm; (*d*) $x = 25.22$ m, $h_0 = 5.5$ cm; (*e*) $x = 25.50$ m, $h_0 = 4.9$ cm; and (*f*) $x = 25.76$ m, $h_0 = 4.0$ cm. Grey line indicates spectrum at the breaking point; cyan line indicates ISZ spectrum at water depth h_0; black line indicates (4.2); red line indicates (4.3). Blue dashed line indicates position of ω_m; red dashed line indicates position of ω_ν.

to 1.99 rad s^{-1}) because large-amplitude infragravity waves favour bore merging (Tissier *et al.* 2017). However, as for the Burgers case (see figure 4), the shape of the energy spectrum at the SW scales, $\omega > \omega_m$, is not affected by low-frequency waves. The diffusive frequency ω_ν, which marks the transition between the inertial and diffusive subranges, increases significantly for BK94-9 (from 18.7 to 24.1 rad s^{-1}) and slightly for vN03-C3 (from 14.9 to 16.1 rad s^{-1}). For both experiments, we observe an increase in the inertial
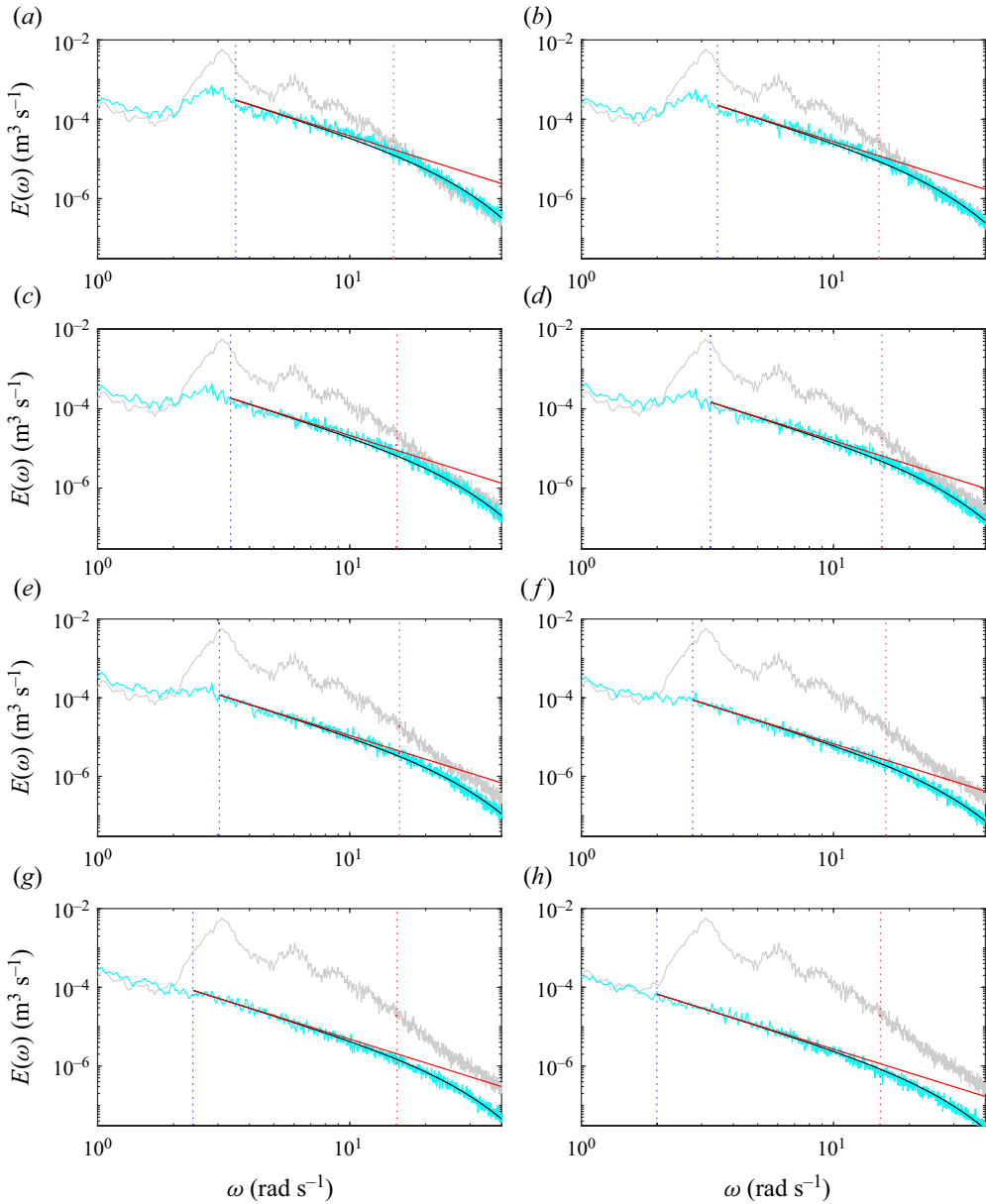
977 A48-16

Figure 8. Energy spectra at different locations in the ISZ for the vN03-C3 experiment: (*a*) gauge 60, $h_0 = 8.4$ cm; (*b*) gauge 61, $h_0 = 7.6$ cm; (*c*) gauge 62, $h_0 = 6.8$ cm; (*d*) gauge 63, $h_0 = 6.1$ cm; (*e*) gauge 64, $h_0 = 5.3$ cm; (*f*) gauge 65, $h_0 = 4.5$ cm; (*g*) gauge 66, $h_0 = 3.7$ cm; and (*h*) gauge 67, $h_0 = 3.0$ cm. Grey line indicates spectrum at the breaking point; cyan line indicates ISZ spectrum at water depth h_0; black line indicates (4.2); red line indicates (4.3). Blue dashed line indicates position of ω_m; red dashed line indicates position of ω_ν.

subrange width as waves propagate, and thus an increase in the Reynolds number R_B. This evolution is observable for all datasets, as can be seen in figure 10. This figure also shows that the Reynolds number is controlled primarily by the peak period T_p of the incident wave field and is an increasing function of T_p. The increase of R_B in decreasing water depth means that the relative importance of nonlinearities with respect to turbulent diffusion
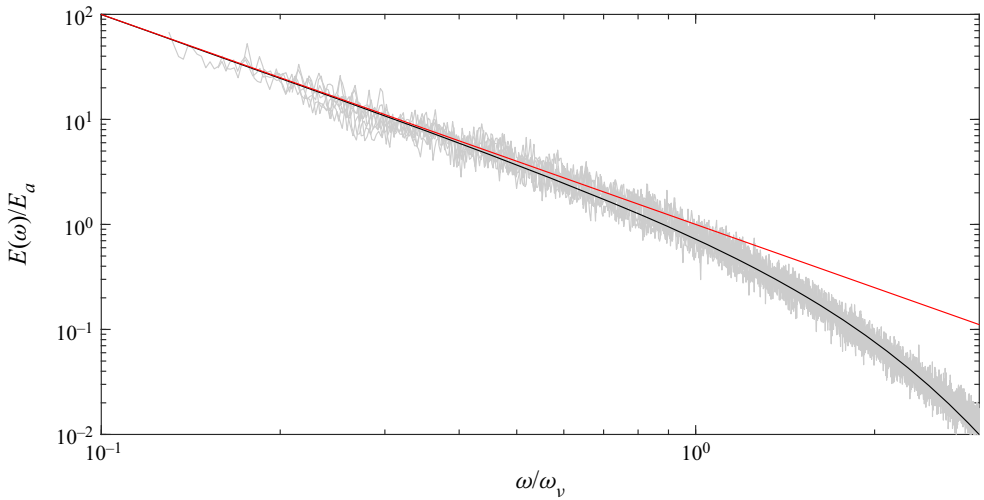
Figure 9. Dimensionless energy spectra E/E_a ($E_a = 8\nu_c^2\omega_m/9g$) at different locations in the ISZ for the vN03-C3 experiment. Grey lines indicate measurements from gauges 60–67 (h_0 from 8.4 cm to 3 cm); black line indicates (5.3); red line indicates ω^{-2} power law.
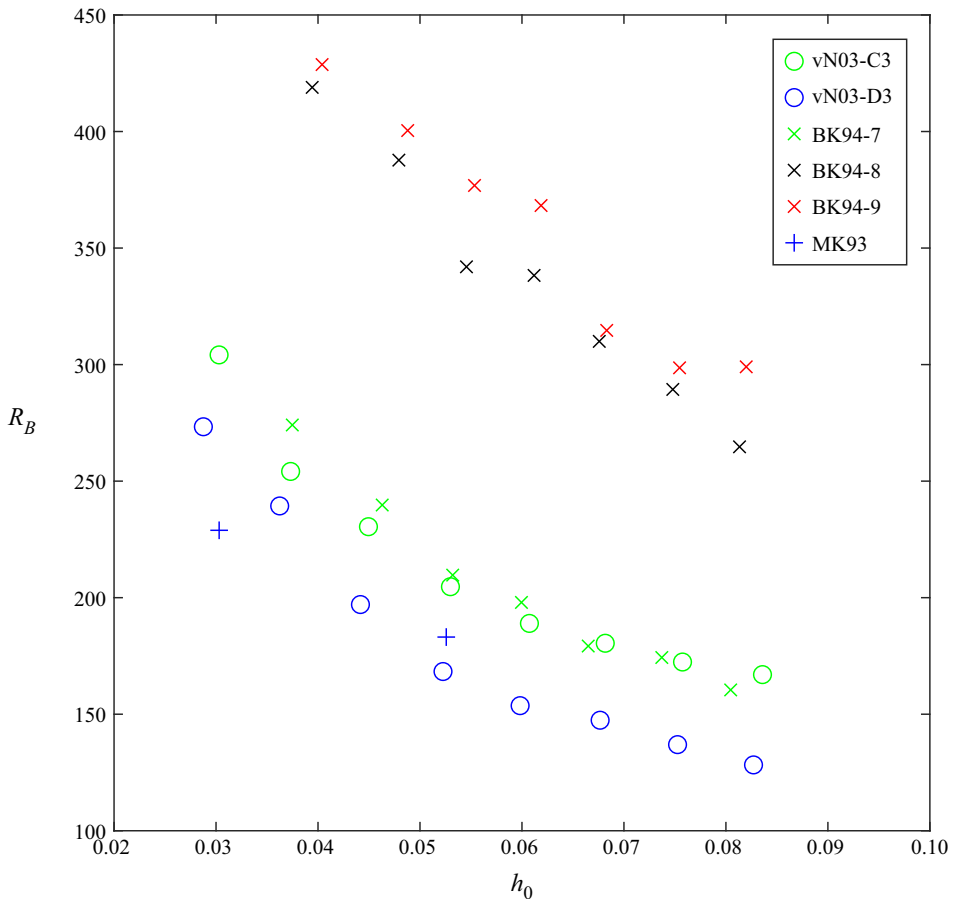

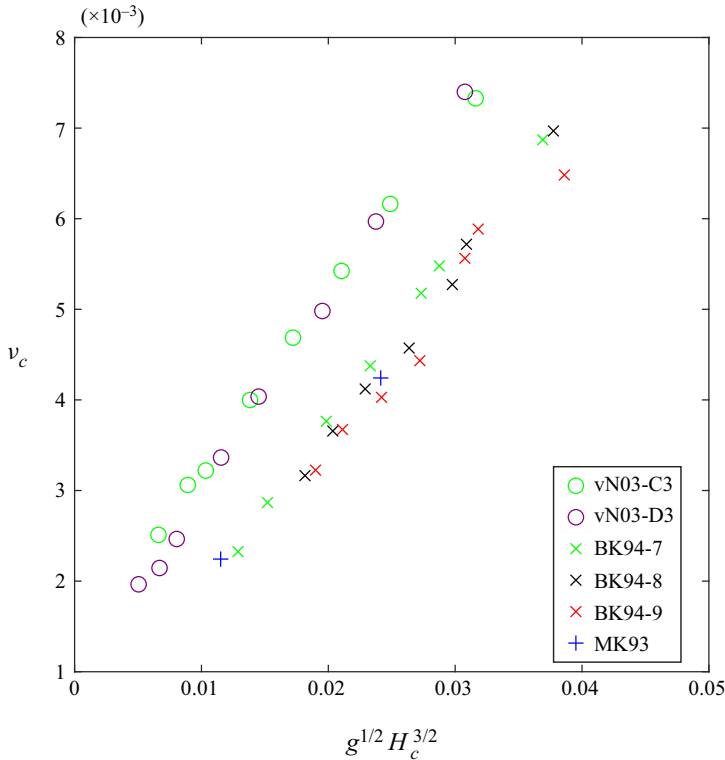Figure 10. Evolution of the Reynolds number R_B as a function of water depth h_0.

Figure 11. Evolution of the diffusion coefficient as a function of $g^{1/2}H_c^{3/2}$.

increases as waves propagate and thus as broken wave height decreases. This differs from what we have observed above for Burgers turbulence, where R_B is an increasing function in H_c. It means that in the ISZ, the characteristic wave height H_c decreases less rapidly than ν_c as h_0 decreases. Assuming that the turbulent diffusion coefficient is controlled mainly by H_c, dimensional analysis leads to the following relationship between ν_c and H_c:

$$\nu_c = \alpha_\nu g^{1/2} H_c^{3/2}, \tag{5.4}$$

where α_ν is a dimensionless coefficient. Similar scalings are used commonly to estimated eddy viscosity in the surf zone (e.g. Svendsen, Schäffer & Hansen 1987). Figure 11 shows that the turbulent diffusion coefficient ν_c follows an $H_c^{3/2}$ power law in agreement with (5.4). However, the value of the coefficient α_ν depends on incident wave conditions. The relation (5.4) implies that R_B evolves approximately as $H_c^{-1/2}T_m$ and is indeed a decreasing function of h_0. It is worth noting that our approach applies only to the ISZ. Indeed, the increase in ν_c with H_c should not be valid in the vicinity of the onset of wave breaking.

6. Energy dissipation

Breaking-wave energy dissipation is one of the most important processes in the nearshore. In particular, it controls the mean wave-induced circulation (Bühler & Jacobson 2001; Bonneton *et al.* 2010). However, wave dissipation in the surf zone remains poorly understood and is modelled heuristically in stochastic spectral wave models (Cavaleri *et al.* 2018). The commonly used method in spectral models is in two steps: first,

total dissipation D is estimated using a parametric random wave model (e.g. Battjes & Janssen 1978; Thornton & Guza 1983) based on an analogy between broken waves and non-diffusive (i.e. $R_B = \infty$) hydraulic jumps; and second, D is redistributed over frequencies following $D(\omega) = \Gamma(\omega) E(\omega)$, where $\Gamma(\omega)$ is an *ad hoc* function satisfying the condition $\int_0^\infty \Gamma(\omega) E(\omega) \, d\omega = D$. In most stochastic spectral models (e.g. operational wave models SWAN and WWIII), Γ is given by the parametrization proposed by Eldeberky & Battjes (1996)

$$\Gamma(\omega) = \frac{D}{E}, \tag{6.1}$$

where E is the total energy.

This method assumes implicitly that D is independent of turbulent diffusion processes at wave fronts and thus independent of the Reynolds number R_B. Even if the dynamics of random SWs in the ISZ is more complex than that of periodic SWs, it is worth noting that for the latter, the dissipation spectrum is strongly dependent on R_B. In the periodic case, it is the sum of D and the nonlinear transfer function T that is nearly independent of R_B and can be approximated by $T(\omega) + D(\omega) = \Gamma E(\omega)$, where $\Gamma = D/E$ (see (3.13)), in a form resembling the parametrization (6.1).

Parametrization (6.1) is also based on the assumption that Γ is independent of ω. However, several studies have shown that Γ is an increasing function of ω (Mase & Kirby 1993; Chen, Guza & Elgar 1997; Elgar *et al.* 1997; Kirby & Kaihatu 1997; Herbers *et al.* 2000; Kaihatu *et al.* 2007; Smit *et al.* 2014). Mase & Kirby (1993) and Elgar *et al.* (1997), based on laboratory and field observations, respectively, identified a frequency-squared tendency for Γ. Mase & Kirby (1993) noticed that this ω^2 dependence appears similar to that of the viscous damping term of the Burgers equation. Kirby & Kaihatu (1997) and Smit *et al.* (2014), by performing numerical simulations with a time-dependent Boussinesq model and a non-hydrostatic model, respectively, confirmed the ω^2 dependence for Γ in the ISZ. In this context, Γ can be written as

$$\Gamma(\omega) = \alpha_\Gamma \omega^2, \tag{6.2}$$

where α_Γ is given by

$$\alpha_\Gamma = \frac{D}{\int_0^\infty \omega^2 E(\omega) \, d\omega}. \tag{6.3}$$

Based on laboratory and field data, Chen *et al.* (1997) demonstrated that spectral Boussinesq model predictions of wave skewness and asymmetry are more accurate with the dissipation parametrization given by (6.2) than by frequency-independent parametrization (6.1).

However, neither parametrization takes into account turbulent diffusion processes at wave fronts. On the other hand, the Burgers-like theory presented in § 4 and validated in § 5 allows us to obtain a relation between $D(\omega)$ and $E(\omega)$,

$$D(\omega) = \frac{2\nu_c}{gh_0} \omega^2 E(\omega), \tag{6.4}$$

which takes into account the turbulent diffusion through ν_c. The frequency-squared dependence of (6.4) is in agreement with observations described just above. We have shown in § 5.2 that the diffusion coefficient is controlled mainly by the characteristic wave height (see (5.4) and figure 11). However, an accurate parametrization of ν_c will require the
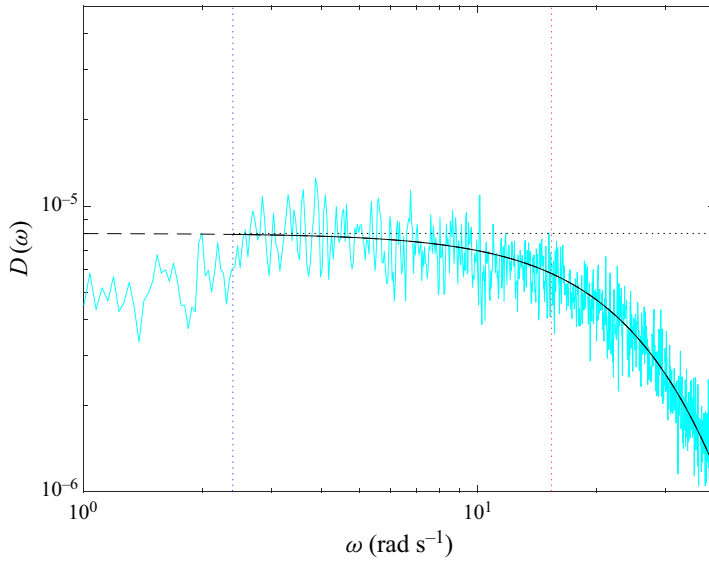
Figure 12. Dissipation spectrum in the ISZ. Cyan line indicates dissipation computed from a measured energy spectrum (see figure 8*g*) and (6.4), vN03-C3 experiment, gauge 66; solid black line indicates theoretical dissipation law (6.6) for $\omega \in [\omega_m, \infty]$; black dashed line indicates theoretical law (6.6) for $\omega \in [0, \omega_m]$, outside of its range of applicability; black dotted line indicates (6.7); blue dotted line indicates position of ω_m; red dotted line indicates position of ω_ν.

analysis of a larger dataset, including field observations. Relation (6.4) does not require an *ad hoc* parametrization of the total dissipation as is the case for previous approaches (cf. (6.1) and (6.2)). On the contrary, $\boldsymbol{D}$ is given explicitly by integrating (6.4) over frequencies, i.e. $\boldsymbol{D} = (2\nu_c/gh_0) \int_0^\infty \omega^2 E(\omega) \, d\omega$. By substituting the energy spectrum equation (4.2) into the last integral, we can obtain an approximate relation for the total dissipation for large R_B:

$$\boldsymbol{D} = \frac{g}{4h_0 T_m} H_c^3. \tag{6.5}$$

If we replace the characteristic wave height H_c by the root-mean-square wave height H_{rms}, this expression is similar to the empirical expression based on an analogy between broken waves and non-diffusive hydraulic jumps (Battjes & Janssen 1978). The approximate relation (6.5) is not useful in itself, but it is very interesting because it highlights a connection between our approach and the classical non-diffusive one (Battjes & Janssen 1978). Equation (6.4) applies only to the ISZ, but it could serve as a theoretical basis for developing new parametrizations of the dissipation spectrum in stochastic spectral models for the entire surf zone.

By combining the energy spectrum law (4.2) and (6.4), we obtain a theoretical law for the dissipation spectrum:

$$D(\omega) = \frac{16}{9} \frac{\nu_c^3}{g^2 h_0} \omega_m \omega^2 \operatorname{csch}^2 \left(\frac{\omega}{\omega_\nu} \right), \quad \omega \in [\omega_m, \infty]. \tag{6.6}$$

The asymptotic form of (6.6) for $\omega \ll \omega_\nu$ is given by

$$D(\omega) = \frac{\nu_c \omega_m H_c^2}{\pi^2 h_0}. \tag{6.7}$$

We now analyse the main characteristics of $D(\omega)$, but without direct experimental validation of theoretical dissipation spectra. A dissipation spectrum computed by applying (6.4) to a measured energy spectrum is presented in figure 12. This dissipation spectrum compares well with the theoretical one in (6.6). We can see that $D(\omega)$ is not proportional to $E(\omega)$ but is nearly constant in the inertial subrange $[\omega_m, \omega_\nu]$, with a value in agreement with (6.7). In other words, there is an equipartition of energy dissipation over the inertial subrange. This result is in agreement with observations by Kirby & Kaihatu (1997) and Kaihatu *et al.* (2007). Kirby & Kaihatu (1997) proposed that this phenomenon arises from the fact that dissipation manifests in the space–time domain as a sequence of isolated spike-like processes. Contrary to energy, dissipation $D(\omega)$ is large up to high frequencies of approximately ω_ν. For example, at large Reynolds numbers ($R_B \sim 400$), the dissipation $D(\omega_\nu)$ is approximately 0.72 times the maximum dissipation $D(\omega_m)$, while the energy ratio $E(\omega_\nu)/E(\omega_m)$ is approximately 10^{-2}. In our datasets, ω_ν can reach values up to $17\omega_p$ (see figure 7*f*). This means that a proper modelling of dissipation needs to consider a frequency range much larger than the one that is sufficient to properly estimate total energy. This is an important result in the context of spectral wave model development.

7. Conclusion

The spectral behaviour of random SWs propagating in the ISZ has been analysed. We show that the elevation spectrum exhibits a universal shape. A theoretical spectrum has been derived based on the similarities between SWs in the ISZ and Burgers SW solutions. Very good agreement between this theoretical model and laboratory experiments covering a large range of incident random wave conditions is shown. The energy spectrum shape is determined by three parameters: $\omega_m = 2\pi/T_m$, the diffusive frequency ω_ν, and the turbulent diffusion coefficient ν_c. It is thus controlled by one dimensionless number defined as $R_B = 4\pi^2(\omega_\nu/\omega_m)$, or equivalently as $R_B = \frac{3}{2}(gH_cT_m/\nu_c)$, where H_c is the characteristic wave height. This Reynolds number quantifies the relative importance of nonlinearities with respect to turbulent diffusion. In the inertial frequency subrange, defined as $\omega \in [\omega_m, \omega_\nu]$, the energy spectrum follows an ω^{-2} tendency. An exponential decay of E with ω is observed in the high-frequency diffusive subrange $\omega \in [\omega_\nu, \infty]$. We have shown that the turbulent diffusion coefficient is controlled mainly by the characteristic wave height, following (5.4). Consequently, the Reynolds number evolves approximately as $H_c^{-1/2}T_m$. The nonlinearities thus increase as waves propagate in decreasing water depth. This explains why the inertial subrange and its ω^{-2} tendency are more marked at the end of the ISZ than at the beginning. It is worth noting that information on turbulent processes in the ISZ can be provided indirectly by applying our theoretical model to high-frequency wave elevation measurements.

In stochastic spectral wave models, it is crucial to have a good parametrization of the dissipation spectrum $D(\omega)$. Within the framework of our theoretical approach, we have derived an explicit relation between D and E (see (6.4)), showing a frequency-squared dependence in agreement with previous laboratory and field studies. Contrary to usual dissipation parametrizations, our relation does not require an empirical estimation of total dissipation D. We must keep in mind that our approach has been developed for the SW regime in the ISZ and not for the entire surf zone. However, our model (6.4) could nevertheless be useful for developing new parametrizations of the dissipation spectrum for the entire surf zone.

An equation has been derived for describing the universal shape of the dissipation spectrum in the ISZ. It highlights that D remains nearly constant within the inertial subrange, and decreases exponentially within the diffusive subrange. The equipartition of dissipation over the inertial subrange is in agreement with previous observations. Contrary to energy, dissipation $D(\omega)$ is large up to high frequencies of approximately ω_ν. Consequently, a proper modelling of the dissipation needs to consider a much larger frequency range than the one containing most of the energy. Therefore, to characterize the spectral behaviour of surf zone waves in the field, it is crucial to be able to quantify accurately the surface elevation spectrum at high frequencies, up to approximately 1–2 Hz. Developments on both nonlinear reconstruction of wave elevation from pressure measurements (Bonneton & Lannes 2017; Bonneton *et al.* 2018; Martins *et al.* 2020) and lidar methods (Brodie *et al.* 2015; Martins *et al.* 2017) should help to achieve this goal.

Author ORCIDs.
Ⓓ Philippe Bonneton https://orcid.org/0000-0002-7536-1084.

REFERENCES

BATTJES, J.A. & JANSSEN, J.P.F.M. 1978 Energy loss and set-up due to breaking of random waves. In *Coastal engineering 1978*, pp. 569–587.

BERTIN, X., *et al.* 2018 Infragravity waves: from driving mechanisms to impacts. *Earth-Sci. Rev.* **177**, 774–799.

BONNETON, P. 2007 Modelling of periodic wave transformation in the inner surf zone. *Ocean Engng* **34**, 1459–1471.

BONNETON, P., BRUNEAU, N., CASTELLE, B. & MARCHE, F. 2010 Large-scale vorticity generation due to dissipating waves in the surf zone. *Discr. Contin. Dyn. Syst.* B **13** (4), 729.

BONNETON, P. & LANNES, D. 2017 Recovering water wave elevation from pressure measurements. *J. Fluid Mech.* **833**, 399–429.

BONNETON, P., LANNES, D., MARTINS, K. & MICHALLET, H. 2018 A nonlinear weakly dispersive method for recovering the elevation of irrotational surface waves from pressure measurements. *Coast. Engng* **138**, 1–8.

BOWEN, G.D. & KIRBY, J.T. 1994 *Shoaling and Breaking Random Waves on a 1 : 35 Laboratory Beach*. University of Delaware, Department of Civil Engineering, Center for Applied Coastal Research.

BRODIE, K.L., RAUBENHEIMER, B., ELGAR, S., SLOCUM, R.K. & MCNINCH, J.E. 2015 Lidar and pressure measurements of inner-surfzone waves and setup. *J. Atmos. Ocean. Technol.* **32** (10), 1945–1959.

BÜHLER, O. & JACOBSON, T.E. 2001 Wave-driven currents and vortex dynamics on barred beaches. *J. Fluid Mech.* **449**, 313–339.

BURGERS, J.M. 1948 A mathematical model illustrating the theory of turbulence. In *Advances in Applied Mechanics*, vol. 1, pp. 171–199. Elsevier.

CAVALERI, L., *et al.* 2018 Wave modelling in coastal and inner seas. *Prog. Oceanogr.* **167**, 164–233.

CHEN, Y., GUZA, R.T. & ELGAR, S. 1997 Modeling spectra of breaking surface waves in shallow water. *J. Geophys. Res.* **102** (C11), 25035–25046.

CIENFUEGOS, R., BARTHÉLEMY, E. & BONNETON, P. 2010 A wave-breaking model for Boussinesq-type equations including mass-induced effects. *ASCE J. Waterway Port Coastal Ocean Engng* **136**, 10–26.

DUTYKH, D. & DIAS, F. 2007 Viscous potential free-surface flows in a fluid layer of finite depth. *C. R. Math.* **345** (2), 113–118.

ELDEBERKY, Y. 1996 Nonlinear transformationations of wave spectra in the nearshore zone. Doctoral dissertation, Delft University of Technology, Delft, The Netherlands.

ELDEBERKY, Y. & BATTJES, J.A. 1996 Spectral modeling of wave breaking: application to Boussinesq equations. *J. Geophys. Res.* **101** (C1), 1253–1264.

ELGAR, S. & GUZA, R.T. 1985*a* Shoaling gravity waves: comparisons between field observations, linear theory, and a nonlinear model. *J. Fluid Mech.* **158**, 47–70.

ELGAR, S. & GUZA, R.T. 1985*b* Observations of bispectra of shoaling surface gravity waves. *J. Fluid Mech.* **161**, 425–448.

ELGAR, S., GUZA, R.T., RAUBENHEIMER, B., HERBERS, T.H.C. & GALLAGHER, E.L. 1997 Spectral evolution of shoaling and breaking waves on a barred beach. *J. Geophys. Res.* **102** (C7), 15797–15805.

FORRISTALL, G.Z. 1981 Measurements of a saturated range in ocean wave spectra. *J. Geophys. Res.* **86** (C9), 8075–8084.

FREILICH, M.H. & GUZA, R.T. 1984 Nonlinear effects on shoaling surface gravity waves. *Phil. Trans. R. Soc. Lond.* A **311** (1515), 1–41.

FRISCH, U. & BEC, J. 2002 Burgulence. In *New Trends in Turbulence (Turbulence: Nouveaux Aspects): 31 July–1 September 2000*, pp. 341–383. Springer.

GURBATOV, S.N., RUDENKO, O.V. & SAICHEV, A.I. 2012 *Waves and Structures in Nonlinear Nondispersive Media: General Theory and Applications to Nonlinear Acoustics*. Springer.

HANSEN, C., KATSAROS, K.B., KITAIGORODSKII, S.A. & LARSEN, S.E. 1990 The dissipation range of wind-wave spectra observed on a lake. *J. Phys. Oceanogr.* **20** (9), 1264–1277.

HASSELMANN, K. 1962 On the nonlinear energy transfer in a gravity wave system. Part 1. *J. Fluid Mech.* **12**, 481–500.

HERBERS, T.H.C. & BURTON, M.C. 1997 Nonlinear shoaling of directionally spread waves on a beach. *J. Geophys. Res.* **102** (C9), 21101–21114.

HERBERS, T.H.C., RUSSNOGLE, N.R. & ELGAR, S. 2000 Spectral energy balance of breaking waves within the surf zone. *J. Phys. Oceanogr.* **30** (11), 2723–2737.

KAIHATU, J.M., VEERAMONY, J., EDWARDS, K.L. & KIRBY, J.T. 2007 Asymptotic behavior of frequency and wave number spectra of nearshore shoaling and breaking waves. *J. Geophys. Res.* **112** (C6), C06016.

KIRBY, J.T. & KAIHATU, J.M. 1997 Structure of frequency domain models for random wave breaking. In *Coastal Engineering 1996*, pp. 1144–1155.

KITAIGORODSKII, S.A., KRASITSKII, V.P. & ZASLAVSKII, M.M. 1975 On Phillips' theory of equilibrium range in the spectra of wind-generated gravity waves. *J. Phys. Oceanogr.* **5** (3), 410–420.

KITAIGORODSKII, S.A. 1983 On the theory of the equilibrium range in the spectrum of wind-generated gravity waves. *J. Phys. Oceanogr.* **13** (5), 816–827.

LENAIN, L. & MELVILLE, W.K. 2017 Measurements of the directional spectrum across the equilibrium saturation ranges of wind-generated surface waves. *J. Phys. Oceanogr.* **47** (8), 2123–2138.

MARTINS, K., BLENKINSOPP, C.E., POWER, H.E., BRUDER, B., PULEO, J.A. & BERGSMA, E.W. 2017 High-resolution monitoring of wave transformation in the surf zone using a LiDAR scanner array. *Coast. Engng* **128**, 37–43.

MARTINS, K., BONNETON, P. & MICHALLET, H. 2021 Dispersive characteristics of non-linear waves propagating and breaking over a mildly sloping laboratory beach. *Coast. Engng* **167**, 103917.

MARTINS, K., BONNETON, P., MOURAGUES, A. & CASTELLE, B. 2020 Non-hydrostatic, non-linear processes in the surf zone. *J. Geophys. Res.* **125** (2), e2019JC015521.

MASE, H. & KIRBY, J.T. 1993 Hybrid frequency-domain KdV equation for random wave transformation. In *Coastal Engineering 1992*, pp. 474–487.

VAN NOORLOOS, J.C. 2003 Energy transfer between short wave groups and bound long waves on a plane slope. Master's thesis, Delft University of Technology, Delft, The Netherlands.

NOULLEZ, A., GURBATOV, S.N., AURELL, E. & SIMDYANKIN, S.I. 2005 Global picture of self-similar and non-self-similar decay in Burgers turbulence. *Phys. Rev.* E **71** (5), 056305.

PHILLIPS, O.M. 1958 The equilibrium range in the spectrum of wind-generated waves. *J. Fluid Mech.* **4** (4), 426–434.

REID, W.H. 1956 On the transfer of energy in Burgers' model of turbulence. *Appl. Sci. Res.* A **6** (2), 85–91.

ROMERO, L. & MELVILLE, W.K. 2010 Numerical modeling of fetch-limited waves in the Gulf of Tehuantepec. *J. Phys. Oceanogr.* **40** (3), 466–486.

SAFFMAN, P.G. 1968 Lectures on homogeneous turbulence. In *Topics in Nonlinear Physics* (ed. N.J. Zabusky), pp. 485–614. Springer.

SMIT, P., JANSSEN, T., HOLTHUIJSEN, L. & SMITH, J. 2014 Non-hydrostatic modeling of surf zone wave dynamics. *Coast. Engng* **83**, 36–48.

SMITH, J.M. & VINCENT, C.L. 2003 Equilibrium ranges in surf zone wave spectra. *J. Geophys. Res.* **108** (C11), 3366.

STIVE, M.J. 1984 Energy dissipation in waves breaking on gentle slopes. *Coast. Engng* **8** (2), 99–127.

STOKER, J.J. 1957 *Water Waves*. Interscience Publishers.

SVENDSEN, I.A., MADSEN, P.A. & HANSEN, J.B. 1978 Wave characteristics in the surf zone. In *Coastal Engineering 1978*, pp. 520–539.

SVENDSEN, I.A. & PUTREVU, U. 1996 Surf-zone hydrodynamics. In *Advances in Coastal and Ocean Engineering*, pp. 1–78.

SVENDSEN, I.A., SCHÄFFER, H.A. & HANSEN, J.B. 1987 The interaction between the undertow and the boundary layer flow on a beach. *J. Geophys. Res.* **92** (C11), 11845–11856.

TATSUMI, T. 1969 Nonlinear wave expansion for turbulence in the Burgers' model of a fluid. *Phys. Fluids* **12** (12), 258–254.

THORNTON, E.B. 1977 Rederivation of the saturation range in the frequency spectrum of wind-generated gravity waves. *J. Phys. Oceanogr.* **7** (1), 137–140.

THORNTON, E.B. & GUZA, R.T. 1982 Energy saturation and phase speeds measured on a natural beach. *J. Geophys. Res.* **87** (C12), 9499–9508.

THORNTON, E.B. & GUZA, R.T. 1983 Transformation of wave height distribution. *J. Geophys. Res.* **88** (C10), 5925–5938.

TING, F.C. & KIRBY, J.T. 1996 Dynamics of surf-zone turbulence in a spilling breaker. *Coast. Engng* **27** (3–4), 131–160.

TISSIER, M., BONNETON, P., ALMAR, R., CASTELLE, B., BONNETON, N. & NAHON, A. 2011 Field measurements and non-linear prediction of wave celerity in the surf zone. *Eur. J. Mech. (B/Fluids)* **30** (6), 635–641.

TISSIER, M., BONNETON, P., MICHALLET, H. & RUESSINK, B.G. 2015 Infragravity-wave modulation of short-wave celerity in the surf zone. *J. Geophys. Res.* **120** (10), 6799–6814.

TISSIER, M.F.S., BONNETON, P. & RUESSINK, B.G. 2017 Infragravity waves and bore merging. In *Proceedings of Coastal Dynamics 2017*, pp. 451–460.

TOBA, Y. 1973 Local balance in the air–sea boundary processes. *J. Oceanogr. Soc. Japan* **29** (5), 209–220.

ZAKHAROV, V. 1999 Statistical theory of gravity and capillary waves on the surface of a finite-depth fluid. *Eur. J. Mech. (B/Fluids)* **18** (3), 327–344.

ZAKHAROV, V.E.E. & FILONENKO, N.N. 1966 Energy spectrum for stochastic oscillations of the surface of a liquid. *Dokl. Akad. Nauk* **170** (6), 1292–1295. Russian Academy of Sciences.

<div align="center">

Supplementary material for
Energy and dissipation spectra of waves
propagating in the inner surf zone

Philippe Bonneton

</div>

UMR 5805 EPOC, CNRS - University of Bordeaux, Allée Geoffroy Saint-Hilaire, F-33615 Pessac, France

A Burgers' spectra

A.1 Periodic sawtooth waves

In the non-diffusive case ($\nu = 0$), the periodic SW Burgers solution, $v_i(x,t)$, is given by

$$v_i = \frac{V_J(t)}{2}\left(\frac{2x}{\lambda} - \mathrm{sgn}(x)\right) \qquad x \in [-\frac{\lambda}{2}, \frac{\lambda}{2}] \quad , \tag{1}$$

where λ is the wavelength, $V_J(t) = \frac{V_0}{1+V_0 t/\lambda}$ is the velocity jump across the inviscid shock (located in $x = 0$) and V_0 is the velocity jump at $t = 0$. Khokhlov derived an exact SW solution of the diffusive Burgers' equation (see *Gurbatov et al.* (2012))

$$v = \frac{V_J(t)}{2}\left(\frac{2x}{\lambda} - \tanh\frac{V_J(t)x}{4\nu}\right) . \tag{2}$$

This solution is not periodic, but for large Reynolds numbers it becomes quasi-periodic between $x = -\lambda/2$ and $x = \lambda/2$, with a diffusive front located in $x = 0$.

In figure 1 we present a comparison between the quasi-periodic theoretical solution (2) and the numerical solution of the Burgers' equation based

<div align="center">1</div>

on a Fourier spectral method. We consider the transformation of an initially sinusoidal wave field into a SW field. Figure 1 shows that there is no distinguishable difference between theoretical and numerical SW solutions.
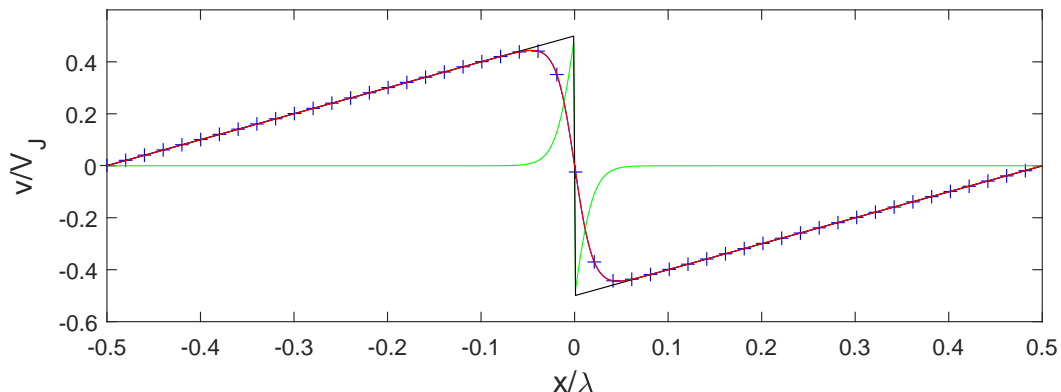

Figure 1: Profile of a periodic Burgers SW at $R_B = 200$. Red line, diffusive solution (equation 2); black line, non-diffusive solution (equation 1); green line, diffusive correction $C = \frac{V_J}{2}\left(-\mathrm{sgn}(x) + \tanh\frac{V_J x}{4\nu}\right)$; +, discrete form (every 10 points) of the numerical solution (Fourier spectral model) of the Burgers' equation at dimensionless time $U_0 t/\lambda = 4.67$ ($R_B = 200$), for a sinusoidal initial condition $v(x, t = 0) = 0.5 U_0 \sin(2\pi/\lambda)$ with $R_B(t = 0) = 1000$.

We will now derive an expression for the SW energy spectrum based on the Khokhlov solution (2). Since v given by this equation is an odd function of x we can expand v as a sine series

$$v(x, t) = \sum_{n=1}^{\infty} v_n(t) \sin(n k_p x) \ ,$$

where $k_p = \frac{2\pi}{\lambda}$ and v_n is the nth Fourier coefficient

$$v_n(t) = \frac{4}{\lambda} \int_0^{\lambda/2} v(x, t) \sin(n k_p x) dx \ .$$

By decomposing the velocity field into $v = v_i - C$, with C the diffusive correction given by $C = \frac{V_J}{2}\left(-\mathrm{sgn}(x) + \tanh\frac{V_J x}{4\nu}\right)$, the Fourier coefficients of the Khokhlov solution (2) can be rewritten as

$$v_n(t) = \frac{4}{\lambda}\left(\int_0^{\lambda/2} V_J(x, t) \sin(n k_p x) dx - \int_0^{\lambda/2} C \sin(n k_p x) dx\right) \ .$$

2

As illustrated in figure 1, the diffusive correction C rapidly decreases to zero as x increases. The upper bound of the second integral can therefore be replaced by ∞. The approximate integral can then be solved by using tables of Fourier transforms (e.g., *Oberhettinger*, 1957). Finally, the Fourier coefficients can be expressed as

$$v_n(t) = -2\nu k_p \mathrm{csch}\left(\frac{2\pi\nu}{V_J}nk_p\right) \,,$$

and the energy spectral density, $\mathcal{E}_{v_n} = \frac{v_n^2}{2}$, as

$$\mathcal{E}_{v_n} = 2\nu^2 k_p^2 \mathrm{csch}^2\left(\frac{k_n}{k_\nu}\right) \,, \tag{3}$$

where $k_n = nk_p$ and $k_\nu = \frac{V_J}{2\pi\nu}$. For $k_n/k_\nu \ll 1$, $\mathcal{E}_{v_n}$ follows a k_n^{-2} power law

$$\mathcal{E}_{v_n} = \frac{2V_J^2}{\lambda^2}k_n^{-2} \,. \tag{4}$$

This last relation is also the exact energy spectral density of the non-diffusive SW solution (1). In the following, the inertial and diffusive subranges will be defined respectively as $k \in [k_p, k_\nu]$ and $k \in [k_\nu, \infty]$. The dimensionless width of the inertial subrange, $(k_\nu - k_p)/k_p$, increases linearly with R_B, since $k_\nu/k_p = R_B/(4\pi^2)$.

We now present a comparison between the theoretical spectrum (3) and spectra obtained from numerical solutions of the Burgers' equation. We consider the transformation of an initially sinusoidal wave field into a SW field. As a sawtooth wave evolves, its velocity jump, and consequently, its Reynolds number decrease. Energy spectra for two Reynolds numbers ($R_B = 200$ and 400) representative of those in the ISZ are presented in figure 2. We can see that there is no distinguishable difference between the theoretical solution (3) and the numerical one. In the inertial subrange the energy spectrum tends to follow the k_n^{-2} power law given by equation (4). The decrease with time in the inertial subrange width, associated with the decrease in R_B, is illustrated in figure 2.
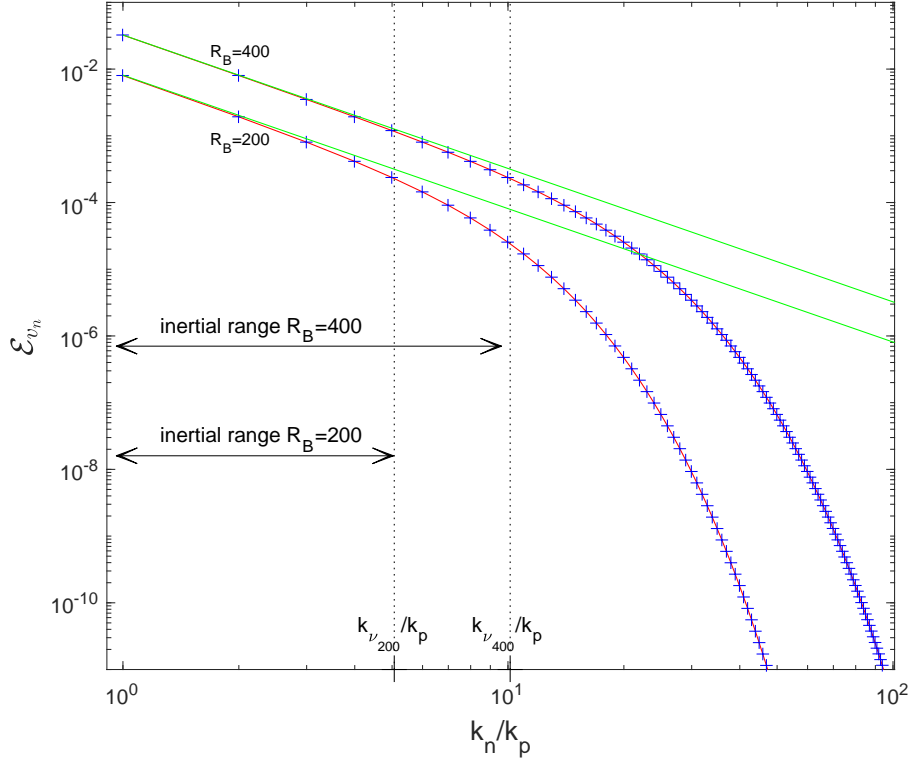
Figure 2: Energy spectral density of periodic Burgers SW at $R_B = 400$ and 200. Red line, diffusive solution (equation (3)); green line, non-diffusive solution (equation (4)); +, numerical solutions of the Burgers' equation at dimensionless times $V_0 t/\lambda = 2.17$ ($R_B = 400$) and $V_0 t/\lambda = 4.67$ ($R_B = 200$), for a sinusoidal initial condition $v(x, t = 0) = 0.5 V_0 \sin (2\pi/\lambda)$ with $R_B(t = 0) = 1000$; dotted lines, positions of k_ν/k_p. For the sake of clarity we use continuous lines to represent the discrete energy spectra (3) and (4).

A.2 Random sawtooth waves

We now consider freely decaying random solutions $v(x,t)$ which are statistically homogeneous in space with zero mean. The power spectral density $\Phi(k,t)$ is the Fourier transform of the auto-correlation function $R(r)$

$$\Phi(k,t) = \frac{1}{2\pi} \int_{-\infty}^{\infty} R(r) \exp(-ikr) dr \ , \tag{5}$$

where $R(r,t) = \langle v(x,t)v(x+r,t) \rangle$. $\Phi(k,t)$ being an even function of k, we limit our analysis to $k \geq 0$ and denote $E_v(k,t) = 2\Phi(k,t)$ the power spectral density function. With this notation, the total energy, $\mathbf{E}_v = \langle v^2 \rangle = \int_{-\infty}^{\infty} \Phi(k)dk$, can be expressed as

$$\mathbf{E}_v = \int_0^{\infty} E_v(k)dk \ .$$

The assumption of isotropy implies $R(-r) = R(r)$ and then

$$E_v(k,t) = \frac{2}{\pi} \int_0^{\infty} R(r) \cos(kr) dr \ . \tag{6}$$

After two integrations by parts equation (6) can be rewritten as

$$E_v(k,t) = \frac{2}{\pi k^2} \int_0^{\infty} \frac{d^2Q}{dr^2} \cos(kr) dr \ , \tag{7}$$

where $Q(x,t) = \frac{1}{2}\langle (v(x+r,t) - v(x,t))^2 \rangle$ and $R(r,t) = \langle v(x,t)^2 \rangle - Q(x,t)$.

In order to estimate $E_v(k,t)$ in the SW regime, *Saffman* (1968) assumed that the periodic solution (2) reproduces the qualitative features of the small-scale behavior of random sawtooth waves. He then found that, for $r \ll \lambda_m$, $Q(r,t)$ can be estimated by

$$Q(r,t) = \frac{V_c(t)^2}{2\lambda_m(t)} \left(r \coth\left(\frac{V_c(t)}{4\nu} r \right) - \frac{4\nu}{V_c(t)} \right) \ , \tag{8}$$

where λ_m is the mean distance between adjacent wave fronts and V_c the characteristic scale of velocity jumps at wave fronts.

By substituing (8) into (7) we obtain

$$E_v(k,t) = \frac{V_c^2}{\pi \lambda_m k^2} \int_0^{\infty} \frac{d^2}{dr^2} (r \coth(\alpha r)) \cos(kr) dr \ ,$$

or

$$E_v(k,t) = \frac{V_c^2}{\pi \lambda_m k^2} \int_0^\infty \frac{d^2\xi}{dr^2} \cos(kr)dr \ ,$$

where $\xi(r) = r(\coth(\alpha r) - 1)$ and $\alpha = \frac{V_c}{4\nu}$. After two integrations by parts

$$E_v(k,t) = \frac{V_c^2}{\pi \lambda_m k^2} F(k) \ ,$$

where

$$F(k) = 1 - k^2 \int_0^\infty \xi(r)\cos(kr)dr \ .$$

$F(k)$ can be written

$$F(k) = 1 - k^2 \frac{dG}{dk} \ ,$$

where $G(k) = \int_0^\infty (\coth(\alpha r) - 1)\sin(kr)dr$.

By using tables of Fourier transforms (e.g., *Oberhettinger*, 1957) we have

$$G(k) = -k^{-1} + \frac{\pi}{2\alpha}\coth(\pi k/(2\alpha))$$

then

$$F(k) = k^2 \frac{\pi^2}{4\alpha^2}\mathrm{csch}^2(\pi k/(2\alpha))$$

and finally

$$E_v(k) = 2\nu^2 k_m \mathrm{csch}^2(2\pi\nu k/V_c) \ .$$

This spectrum law differs slightly from the *Saffman* (1968) law

$$E_S(k) = \frac{2\pi\nu^2}{L}\mathrm{csch}^2(\pi\nu k/(2V_c)) \ ,$$

where Saffman defined L as the *averaged distance* between wave fronts (i.e., λ_m). We have shown that in fact $L = \lambda_m/2$. We have also corrected a typo in the csch-term.

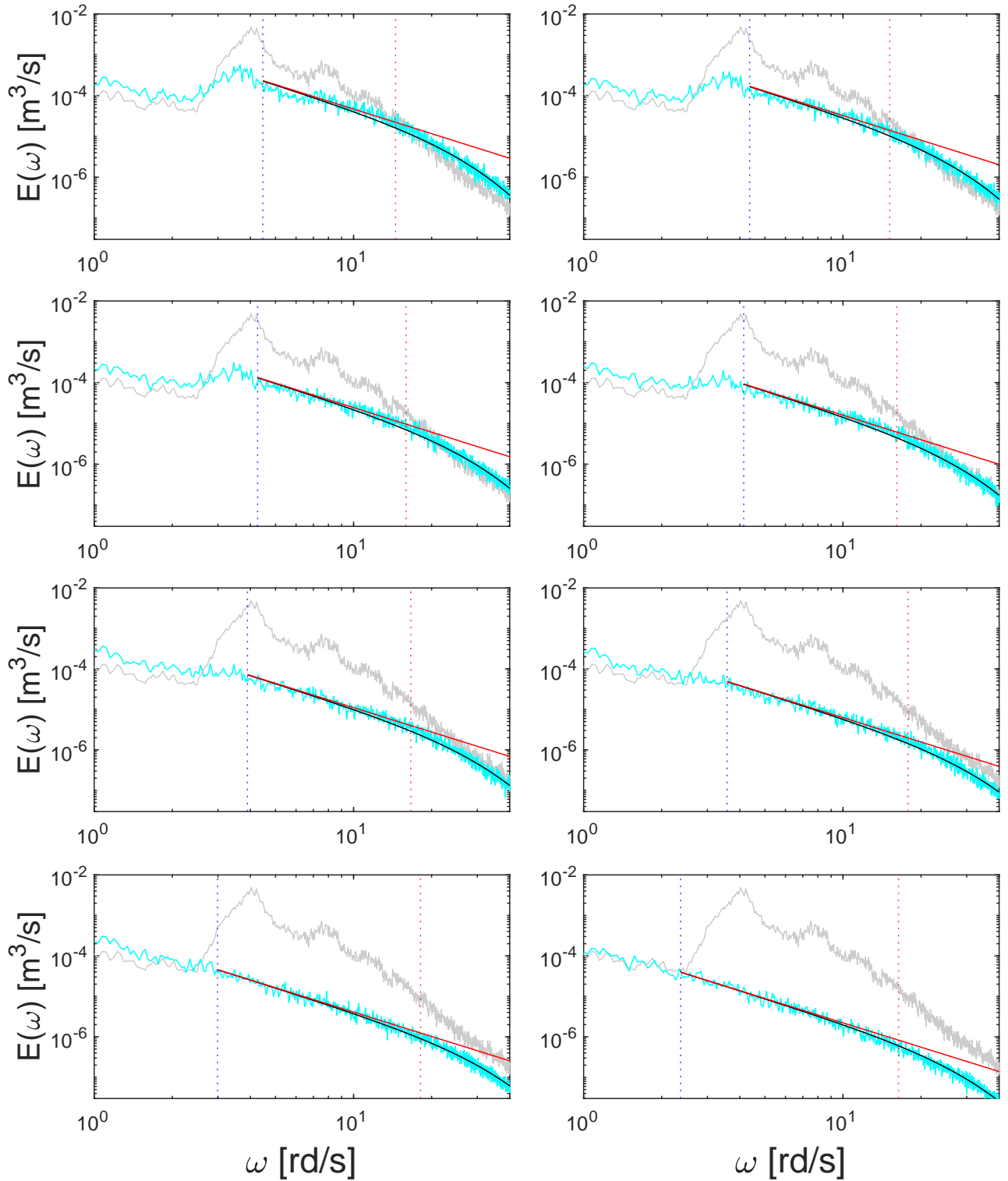# B Additional ISZ energy spectra

6

Figure 3: Energy spectra at different locations in the ISZ for the vN03-D3 experiment. a, gauge 62, $h_0 = 6.8$ cm; b, gauge 63, $h_0 = 6.0$ cm; c, gauge 64, $h_0 = 5.2$ cm; d, gauge 65, $h_0 = 4.4$ cm; e, gauge 66, $h_0 = 3.6$ cm; f, gauge 67, $h_0 = 2.9$ cm. Grey line, spectrum at the breaking point; cyan line, ISZ spectrum at water depth h_0; black line, equation (4.2); red line, equation (4.3). Blue dashed line, position of ω_m; red dashed line, position of ω_ν.
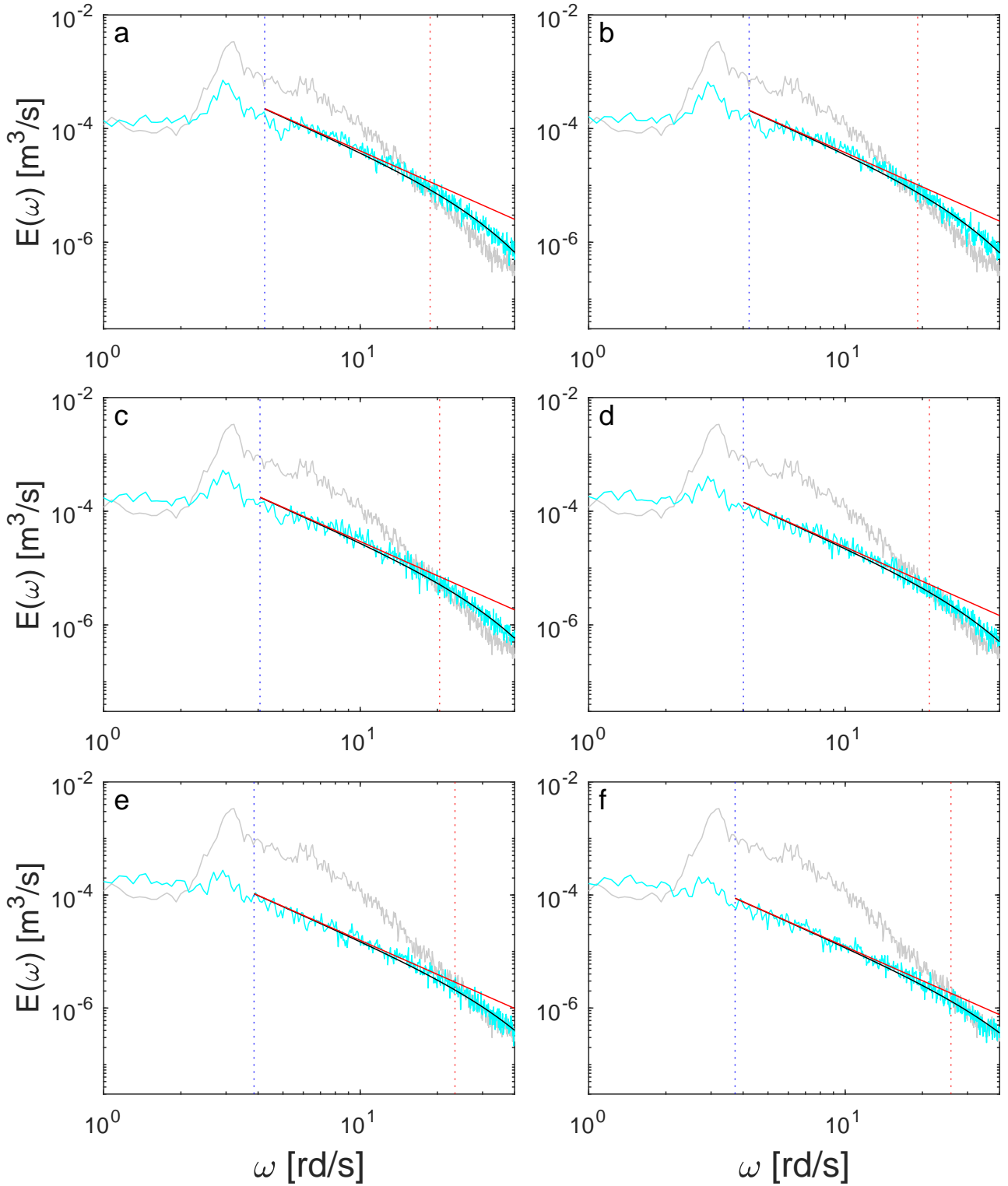
Figure 4: Energy spectra at different locations in the ISZ for the BK94-7 experiment. a, $x = 24.50$ m, $h_0 = 7.4$ cm; b, $x = 24.72$ m, $h_0 = 6.7$ cm; c, $x = 24.97$ m, $h_0 = 6.0$ cm; d, $x = 25.22$ m, $h_0 = 5.3$ cm; e, $x = 25.50$ m, $h_0 = 4.6$ cm; f, $x = 25.76$ m, $h_0 = 3.8$ cm. Grey line, spectrum at the breaking point; cyan line, ISZ spectrum at water depth h_0; black line, equation (4.2); red line, equation (4.3). Blue dashed line, position of ω_m; red dashed line, position of ω_ν.
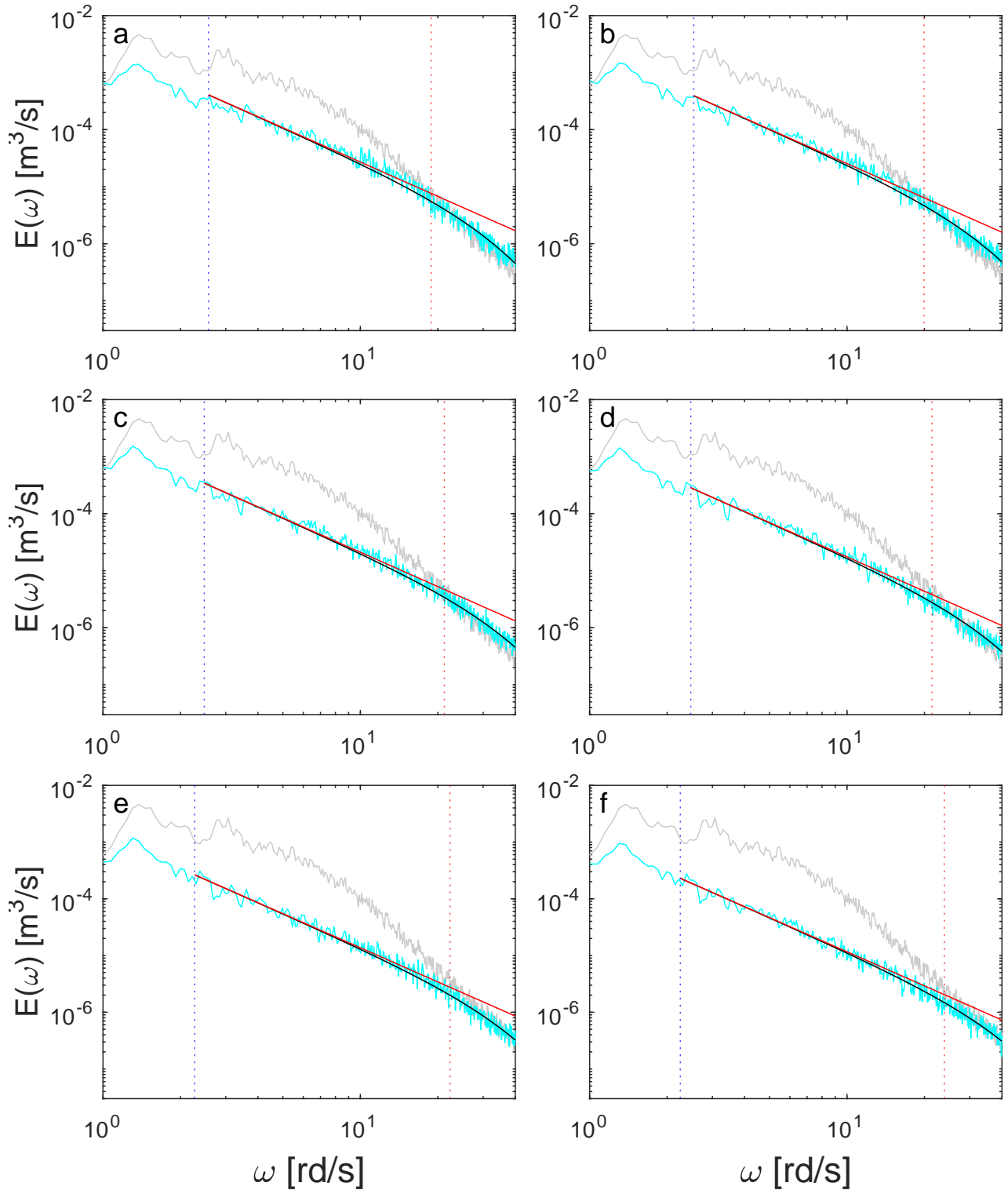
Figure 5: Energy spectra at different locations in the ISZ for the BK94-8 experiment. a, $x = 24.50$ m, $h_0 = 7.5$ cm; b, $x = 24.72$ m, $h_0 = 6.8$ cm; c, $x = 24.97$ m, $h_0 = 6.1$ cm; d, $x = 25.22$ m, $h_0 = 5.5$ cm; e, $x = 25.50$ m, $h_0 = 4.8$ cm; f, $x = 25.76$ m, $h_0 = 3.9$ cm. Grey line, spectrum at the breaking point; cyan line, ISZ spectrum at water depth h_0; black line, equation (4.2); red line, equation (4.3). Blue dashed line, position of ω_m; red dashed line, position of ω_ν.
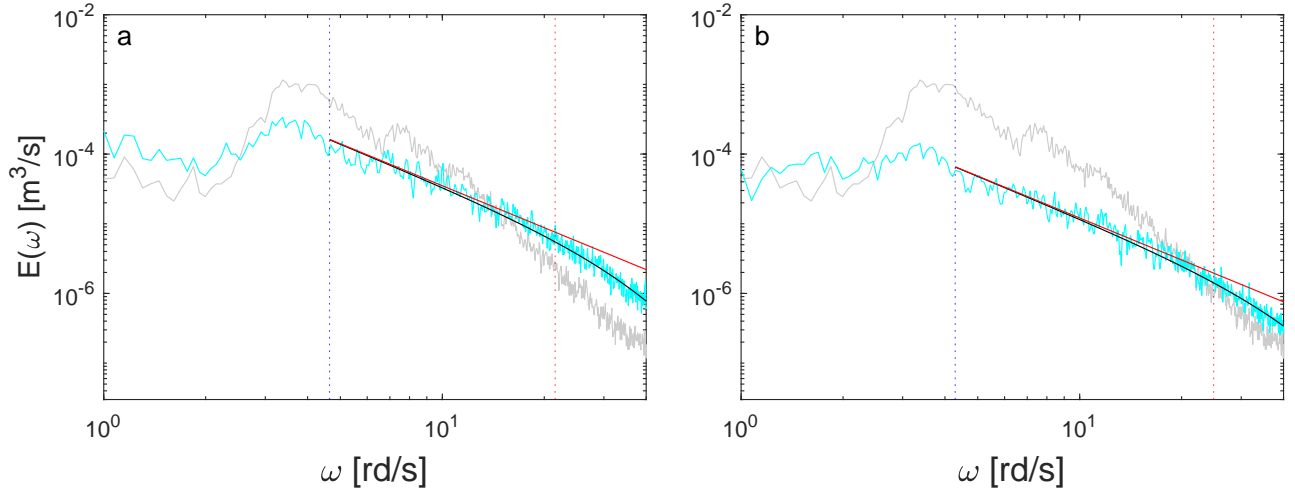
9

Figure 6: Energy spectra at 2 locations in the ISZ for the MK93 experiment. a, gauge 10, $h_0 = 5.3$ cm; b, gauge 11, $h_0 = 3.5$ cm. Grey line, spectrum at the breaking point; cyan line, ISZ spectrum at water depth h_0; black line, equation (4.2); red line, equation (4.3). Blue dashed line, position of ω_m; red dashed line, position of ω_ν.

References

Gurbatov, S. N., Rudenko, O. V., and Saichev, A. I. (2012). Waves and structures in nonlinear nondispersive media: general theory and applications to nonlinear acoustics. *Springer Science & Business Media*.

Oberhettinger, F. (1957). Tabellen zur Fourier transformation. Springer-Verlag.

Saffman, P. G. (1968). Lectures on homogeneous turbulence. *Topics in nonlinear physics*, ed. N.J. Zabusky. New York: Springer, 485-614.